CAPILLARY PRESSURE IN NANOPORES: DEVIATION FROM YOUNG-LAPLACE EQUATION

A Thesis

by

BO LI

Submitted to the Office of Graduate and Professional Studies of
Texas A&M University
in partial fulfillment of the requirements for the degree of

MASTER OF SCIENCE

Chair of Committee,	I. Yucel Akkutlu
Committee Members,	Khoa Bui
	Lisa M. Perez
Head of Department,	A. Daniel Hill

May 2017

Major Subject: Petroleum Engineering

ABSTRACT

Recent studies on multi-phase fluids in nanoscale capillaries indicated that the capillary wall-fluid interactions could play a dominant role on the co-existence of the phases, which caused the fundamental properties of the fluids, such as density, viscosity, and interfacial tension, to become capillary size-dependent. At the extreme of the confinement, these properties become vague. This raises a serious question on the validity of Young-Laplace equation to predict capillary pressure in small capillaries that the unconventional resources commonly exhibit. In this research, using non-equilibrium molecular dynamics simulation of mercury injection into model nano-capillaries, the nature of multi-phase fluids is investigated in capillaries with sizes below 20 nm and the Young-Laplace equation is re-visited.

Higher capillary pressure is predicted for the model nano-capillaries used in the simulations compared to that value obtained using the Young-Laplace equation, in particular, when the capillary diameter is less than 10nm. Good agreement found with the theory in larger size capillary. The capillary pressure increases as the capillary size decreases and shows a power-law dependence on the size of the capillary. This dependence yields up to 70% increase in the estimated capillary pressure value for the extreme case of 1nm capillary. Higher tangential local pressure resulted from the adsorption phase, which identified as the cause of this difference. Two approaches were used for the capillary pressure calculation from the molecular dynamics simulation and the more reliable one was used for further evaluation.

Based on the observations, a modified Young-Laplace equation is proposed for mercury-air filled pore systems which are commonly used in Mercury Injection Capillary Pressure (MICP) experiments for the pore volume and pore size distribution (PSD) measurements. At the highest injection pressure of MICP, the minimum captured pore throat size is predicted 4.8nm instead of 3.6nm based on the Young-Laplace equation. The increase in the predicted capillary size leads to an increase in total pore volume of the sample. The error is up to 20% for measurements with shale samples. The results are important for the characterization of resource shale formations because the pore volume correction influence the hydrocarbon in-place and reserve calculations.

The work can be extended to other multi-phase systems, such as oil-water and water-gas, grouping with other capillary wall material to study the behavior of multi-phase flow in nano-capillaries.

ACKNOWLEDGEMENTS

I would like to thank my committee chair, Dr. I. Yucel Akkutlu, and my committee members, Dr. Khoa Bui and Dr. Lisa M. Perez, for their guidance and support throughout the course of this research.

Thanks also go to my friends and colleagues and the department faculty and staff for making my time at Texas A&M University a great experience.

Finally, thanks to my parents for their encouragement and motivation for me to select this major and pursue my master of science degree.

CONTRIBUTORS AND FUNDING SOURCES

This work was supervised by a thesis committee consisting of Dr. I. Yucel Akkutlu, Dr. Khoa Bui, and Dr. A. Daniel Hill of the Department of Petroleum Engineering, and Dr. Lisa M. Perez of the Department of Chemistry.

The example input file for Molecular Dynamic simulation was provided by Dr. Khoa Bui.

All other work conducted for the thesis was completed by the student independently.

NOMENCLATURE

σ	Surface Tension
ε	Depth of the Potential Well
σ_{Hg-C}	Length Scale of Mercury-Carbon Interaction
ϕ	Porosity
θ	Contact Angle
U (or Φ)	Mutual Potential Energy
a	Constant in the Modified Young-Laplace Equation
b	Constant in the Modified Young-Laplace Equation
F	Unit of Electrical Capacitance, Farad
g	Gravitational Acceleration
G	Correction Term for the Young-Laplace Equation
MICP	Mercury Injection Capillary Pressure
MC	Monte Carlo
MD	Molecular Dynamics
NMR	Nuclear Magnetic Resonance
P_c	Capillary Pressure
PSD	Pore Size Distribution
r	Radius of the Capillary Tube
R	Dimensionless Radius
SANS	Small-angle Neutron Scattering

SAXS   Small-angle X-ray Scattering

SEM   Scanning Electron Microscopy

TABLE OF CONTENTS

LIST OF FIGURES

LIST OF TABLES

CHAPTER I

INTRODUCTION

This thesis is on accurate characterization of resource shale pore structure using Mercury Injection Capillary Pressure (MICP) method. This method has been widely used in the industry to measure the pore size distribution and predict the interconnected pore volume using the fundamental theory of mercury-air displacement based on the Young-Laplace equation. According to the theory, mercury is expected to invade a particular size capillary in the network and displace the air therein only when the mercury is forced into the capillary beyond the capillary pressure threshold. The equation gives exactly the threshold pressure necessary for the intrusion. However, with the resource shale, the concern is the tight nature of the formation with capillaries having sizes down to nanometer. In such small capillaries, the threshold pressure that needs to be overcome increases dramatically. Hence, MICP has injection limit to force mercury into the shale samples and detect nanopores. In addition, at extreme pressure and pore size conditions it is possible that the theory collapse due to changes in the properties of the mercury and the mercury-air system such as density, interfacial tension, and contact angle. In the latter case, the pore size distribution and total pore volume of the shale sample could be measured incorrectly.

As the fundamental theory giving the injection pressure-capillary size relationship for MICP experiment, the Young-Laplace equation and its application to MICP has recently become questionable. In this study, the Molecular Dynamics (MD)

simulation method is used to re-visit the capillary pressure theory based on the Young-Laplace equation in pores below 20nm. A piston model is developed to simulate mercury injection under extreme conditions. The study shows clearly the current limitation of the experimental method, and proposes a modified Young-Laplace equation based on the simulation results. This work is important in gaining new insights into MICP method to have accurate measurement of shale matrix properties such as pore size distribution, total pore volume, and porosity. In addition, the study helps us understand the displacement processes in nanocapillaries and to explore the multi-phase flow behavior in nanoporous materials.

1.1   Background

Previous investigations in our group on resource shale hydrocarbon in-place and reserve calculations showed dependence of the fluid storage and transport mechanisms to the pore size distribution of the formation (Akkutlu and Fathi, 2012; Rahmani and Akkutlu, 2013; Kou et al., 2016; Bui and Akkutlu, 2016). Hence, to predict the reservoir properties, such as effective porosity and permeability, accurate measurement of the pore size distribution of the formation is critical. However, pore size measurements using shale samples is relatively poor due to presence of a wide distribution. Resource shales have organic (kerogen) pores, inorganic pores, micro-cracks and fractures with sizes spanning several orders of magnitude in length (Loucks et al., 2009; Loucks et al., 2012). Resource shale could have small pores, rather macromolecular openings, in solid kerogen down to a few angstroms (A).

2

In general, the pores are categorized based on their size using the International Union of Pure and Applied Chemistry (IUPAC) notation as follows:

- micropores with sizes less than 2nm;

- mesopores with sizes in between 2-50nm;

- macropores with sizes larger than 50nm.

Shale samples obtained from the currently existing resource shale basins in North America often contain pores from all of the categories above. Bustin et al., (2008), for example, used several pore size measurement techniques and predicted that the typical mode of the measured pore size distribution of the samples from the Barnett and Antrim shale formations were around 10nm and others around 10 μm. Adesida et al. (2011) later on reported crushed Barnett shale samples with 20-40% of the pore volume consisting of pores with sizes below 10nm. Similarly, Kuila and Prasat (2013) reported the existence of the nanopore size distribution for various shale samples. These investigations independently indicated that resource shales could be considered as a naturally-occurring nanoporous materials. Typically, two types of nanopores are observed in shale: the inter-particle pores, which exist in between the small grains, and the intra-particle organic pores which are located within the solid kerogen (Loucks et al., 2009). The inter-particle nanopores, also known as clay pores, are often taken by the formation water (i.e., the clay-bound water) and do not permit significant storage of hydrocarbons; however, the intra-particle pores, often associated with the kerogen nanopores are places for hydrocarbon storage.

1.2   Techniques for Pore Size Distribution Measurements

Several techniques have been considered to measure the nanopore size

distribution of shale. These include mercury injection capillary pressure (MICP) method,

low-pressure cryogenic adsorption method, nuclear magnetic resonance (NMR)

spectrometry, scanning electron microscopy (SEM), and small-angle scattering methods.

The first two methods involve a measurement fluid (e.g., mercury, nitrogen, carbon

dioxide) and based on penetration of the measurement fluid into the sample through an

interconnected network of pores and throats; whereas the other methods involve signals

with ability to penetrate through the solid and, hence, measure the total pore volume. In

cryogenic adsorption method, N_2 or CO_2 is introduced at a fixed low temperature into

the sample and the fluid pressure is varied below the saturation pressure of the fluid.

Ramping up the pressure leads to adsorption and capillary condensation of the fluid

inside the pores; whereas ramping the pressure down leads to desorption of the fluid.

The constructed adsorption-desorption curves are then converted to pore size, specific

surface area, and pore geometry. CO_2 adsorption is useful for measuring and

characterizing micropores, while N_2 is suitable for measuring mesopores and macro-

pores (Josh et al., 2012; Clarkson et al., 2013; Sigal, 2015). However, this method has a

relatively low range of measurement, with an upper limit of about 300nm or 0.3μm

(Clarkson et al., 2011). NMR spectrometer, on the other hand, creates permanent and

pulsating magnetic fields and records the relaxation times of the fluid-saturated sample

protons. The contrast in the relaxation times of the pore fluids versus solid skeleton

creates an important measure to provide the pore volume of samples (Coates et al.,

1991). With the smaller pores the protons of the fluid relax faster, hence the rate of relaxation becomes a measure of the pore size distribution. SEM is a destructive method that produces high-resolution 2D and 3D images of the samples and allows estimation of the porosity, pore connectivity and permeability from the images. This method can capture pores as small as 4-6nm. Recent studies showed that for materials with a large pore size distribution such as shale, it is beneficial to combine multiple technique, e.g., NMR and gas injection methods, and develop hybrid methods for the investigation of the complete pore size distribution (Coates et al., 1999, Bustin et al., 2008 and Josh et al., 2012; Sigal 2015). Finally, small-angle neutron-scattering (SANS) and x-ray scattering (SAXS) methods involve scattering of the beam that is directed at the sample in small angles to investigate its structure (Clarkson et al., 2013).

1.3   Capillary Pressure

The multi-phase flow in oil and natural gas production involves co-existence and transport of oil, water and gas. During the oil or gas production, the multiphase flow in porous media is common. It occurs frequently in the gas production when the reservoir pressure is decreased. It is also common during waterflooding or enhanced oil recovery operations.

When two immiscible phases meet in a capillary, they are separated with an interface. The pressure difference across the interface is defined as the capillary pressure. This is the pressure that has to be overcome by the displacing phase in order to

flow. The well-known Young-Laplace equation defines the capillary pressure as a function of the capillary radius:

$$P_c = \frac{2\gamma cos\theta}{r} \tag{1}$$

where, P_c represents the required capillary pressure of the two phases, γ the interfacial tension between the two phases, θ the contact angle, and r the capillary radius. The detailed derivation of this equation is included in Appendix A using the capillary rise problem. The contact angle quantifies the wettability of the wall surfaces of the capillary, which is commonly measured as the liquid-vapor interface on a specific surface. Both strongly water-wet or oil-wet reservoirs exist globally although the water-wet reservoirs are more common. When the wetting phase is displacing the non-wetting phase, the saturation of the wetting phase increases; this process is known as imbibition. On the other hand, the wetting phase decrease is defined as the drainage process. During MICP measurement mercury penetration into an air-filled rock under vacuum is considered as a drainage process because mercury is always the nonwetting phase.

1.4 Mercury Injection Capillary Pressure (MICP)

Among the measurement techniques, MICP is the most traditional approach for the pore volume and pore size distribution measurements. It was first proposed by Washburn (1921) to measure the capillary pressure-liquid saturation curve. Later, it was introduced by Purcell (1949) as an approach for measuring the pore size distribution of rock samples. Prior to begin the experiment, the samples should be cleaned and the

residual fluid molecules inside the pores such as the adsorbed water or hydrocarbons should be removed from the core sample. This is typically done keeping the samples under vacuum over extended time. During the measurement, liquid mercury, being the ultimate non-wetting phase to any sedimentary rock sample, is forced into the sample using a piston. This is the drainage process where the residual air left in the pore network is displaced by the mercury. The injection pressure applied by the piston is increased in small steps with equal size. The pressure steps are recorded up to six significant figures to increase the accuracy and resolution of the pore size distribution measurement. The injected volume of mercury is monitored at each pressure step, and the volumetric pore size distribution as a result is obtained from the raw data of the intrusion volume versus pressure. The higher pressure the piston applies, the smaller void in the sample the mercury invades. However, significantly high pressure is required during the process of mercury intrusion into small pores. With the current technology, the experimental setup can achieve as high as 60,000 psia (0.4GPa). This method is based on the assumption that the pores inside the sample are interconnected, and the original pore geometry will not be changed during the mercury intrusion (Abell et al., 1999).

Liquid mercury intrudes into the target pore when the pressure applied to the piston is equal or larger than the capillary pressure required to displace air in that pore. This capillary pressure value is predicted for a given radius using the Young-Laplace equation (Equation 1), which requires *a priori* mercury-air interfacial tension and contact angle, based on the assumption that the pore geometry in the core sample is cylindrical. Industry commonly uses 480mN/m and 140° as the values of γ and θ,

respectively. Indeed, the surface tension and contact angle used in the Young-Laplace equation are sensitive to the solid wall material. A recent experimental study using graphite predicted a contact angle as high as 152.5±2° at room temperature (Awasthi et al., 1996). This value also agreed with the measurement by Chen et al. (2005) using molecular dynamics simulation. In this thesis, because the wall of our capillary model is made of graphene, which represents a highly-mature kerogen in shale, the value of 152.5° was used for the contact angle. In addition, we used γ value of 475.5 mN/m, which was measured by Wang et al., (2016) using Lu-Jiang model (2005) as for the graphene surface.

In pore networks characterized by pores that are interconnected with throats, it is argued that MICP measures the pore throat size distribution of the sample, rather than the sizes of the pores (Keighin, 1997; Clarkson et al., 2013). By definition, the sizes of the throats are smaller than the pores, except for the slit-shape pores, and usually has a measurable and consistent ratio found in carbonates and sandstones (Coates et al., 1999; Josh et al., 2012). Consequently, in the sedimentary rocks, MICP is known to measure a pore size distribution that is shifted to the smaller end. Nevertheless, this method is widely used because it has relatively a large measurement range, 0.003 to 500 μm, and it also takes short measurement time about only half an hour to finish the analysis (Rigby and Edler, 2002; Giesche, 2006). As a result, it is also a relatively less expensive approach. Some literatures proposed that the upper end of the measuring range using MICP is as high as a few hundred micrometers (Giesche, 2006; Rigby and Edler, 2002; Wang et al., 2016), but usually the minimum captured pressure through the experiment

is 0.5 psi or higher, which has the corresponding diameter of 428µm based on the

Young-Laplace equation.

As for shale pore throat size distribution, which varies in 4 to 5 orders of

magnitude, MICP measurements yield a significantly larger range than any other

techniques introduced before. MICP also plays an important role in determining the

permeability of shale (Apisaksirikul, 2016), together with NMR relaxation time (Rezaee

et al., 2012).

1.5 Local Pressure Calculation in Nanopores

Note that the Young-Laplace equation considers the pressure difference across

the interface based on the average pressure. The average pressure is the arithmetic

average of the three individual compressional stresses:

$$p = \frac{1}{3}(p_{xx} + p_{yy} + p_{zz}) \tag{2}$$

where, $p_{xx}=p_{yy}$, are the tangential pressures and p_{zz} is the pressure normal to the interface.

Hence, the pressure we commonly use in the calculations is in fact the average of the

diagonal terms of the stress tensor. Away from the interface, the fluid is isotropic.

Hence, these three components have the same value. Consequently, the pressure is

uniform and equal to the arithmetic average of the components. However, near the

interface anisotropy develops. Interfacial tension is a consequence of this anisotropy in

the compressional stress field. In previous work (Bui and Akkutlu, 2015; Bui and

Akkutlu, 2016) showed that added complexity occurs in the local pressure (as well as
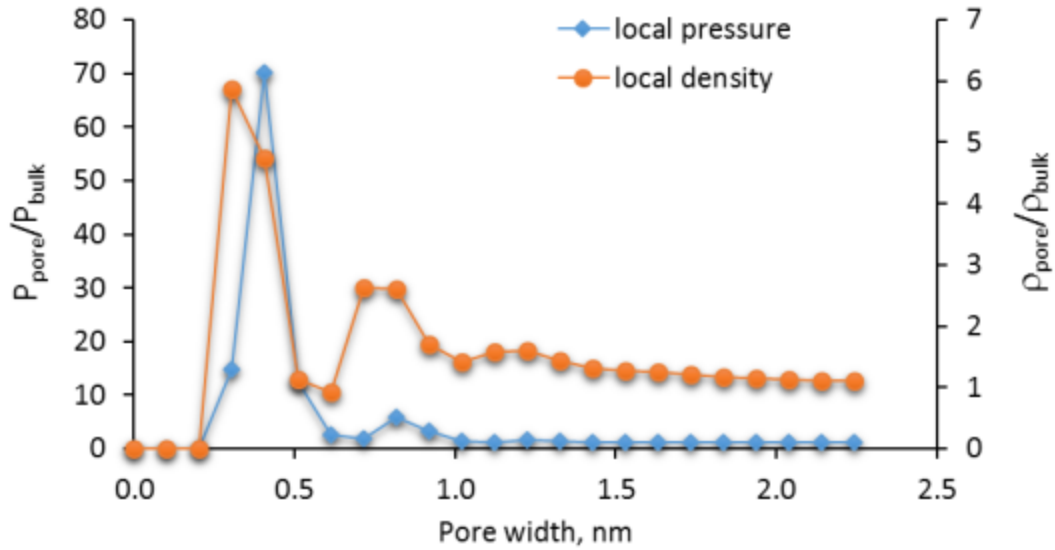
Figure 1 Local pressure and density across the width of a 4.4nm channel as a function of distance from the wall. The pressure and density inside the channel are normalized by the values of a bulk fluid that is in equilibrium with the channel at 138 bars. Adapted from Bui and Akkutlu (2016).

density) of a fluid inside a nanopore. These quantities become strongly heterogeneous (Figure 1). In addition, the local pressure is strongly anisotropic inside the pore, $p_{xx}=p_{yy} \gg p_{zz}$. The heterogeneity and anisotropy in pressure is due to amplified fluid-wall interactions, namely physical adsorption: More specifically, the extreme local pressure within the adsorbed layer by the wall is caused by the tangential stress components, while the normal stress remains constant across the diameter of the pore. Consequently, the average pore pressure becomes pore-wall and -size dependent. This observation is important to our work because, an increase in the average pore pressure due to anisotropy is an increase in pressure at the pore entry during the MICP measurement of small pores. The analysis of the MICP data does not consider the entry effects, however.

The heterogeneity in local quantities and the anisotropy in local pressure could be much more amplified in small pores, where volume for free fluid is reduced, such that behavior of the mercury-air interface at the entrance of a pore could change dramatically. This change in interfacial behavior could be perceived as a change in the values of the interfacial tension and the contact angle. For example, Bui and Akkutlu (2015) reported the interfacial tension of a liquid-vapor interface in nanopores is significantly reduced as the pore size is decreased. Thus, MICP measurements involving samples with small pores have these added molecular level complexities.

Previous work related to the applicability of Young-Place equation in nanopores has found that both the contact angle and the interfacial tension are pore size dependent. The pore size effects were found to be significant in sub-10nm pores, where with respect to the conventional values of 152.5° and 475.5 mN/m for graphene surface, the contact angle was increased as the pore size decreased (Wang et al., 2001; Werder et al., 2003; Kutana and Giapis, 2007 and Wang et al., 2016), and the surface tension was also found varying with the pore size and the curvature (Tolman, 1949). The latter has established the Gibbs-Tolman-Koenig-Buff (GTKB) equation for the curvature-dependent surface tension. However, due to the limited understanding of the Tolman's length in this equation, Lu and Jiang (2005), and Kalová and Mareš (2015) later indicated theoretical models based on GTKB equation. Using Lu-Jiang's (2005) model, Wang et al. (2016) found that the surface tension dropped sharply when the capillary radius less than 20nm. These studies adopted the Young-Laplace equation, where the surface tension or contact angle were corrected for the nanopore size.

11
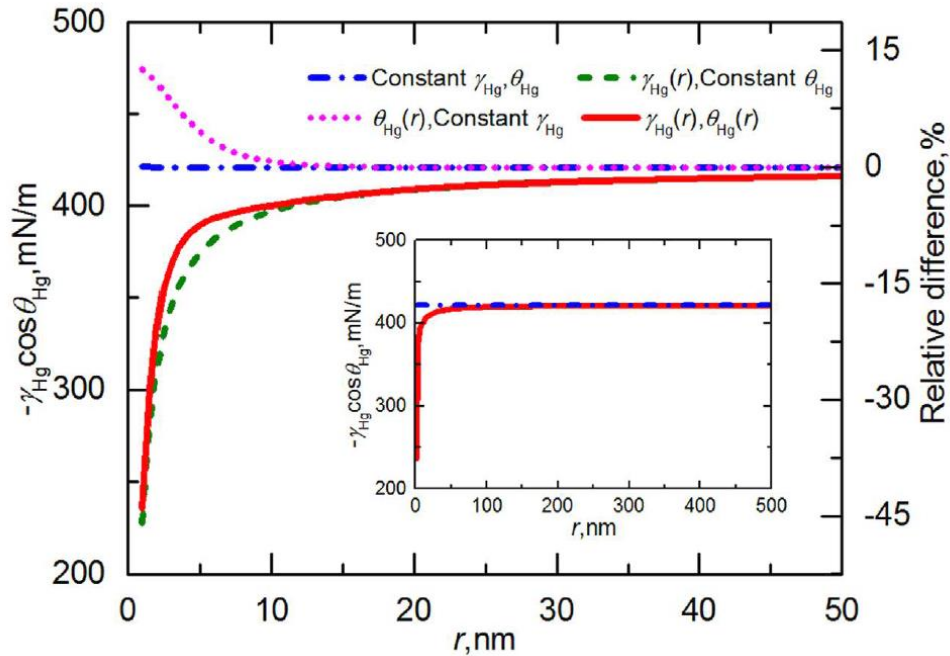
Figure 2 Surface tension and contact angle measurement results as a function of pore radius r. With added (r) after the parameter, they are considered size-dependent. The blue dash line is showing the multiply using scalar value of contact angle and surface tension, while the other lines represent different groups with size-dependent parameters. Adapted from Wang et al. (2016).

Among the previous work related to study the capillary pressure in nanopores, Wang et al. (2016) gave the first study of the size-dependence of contact angle and surface tension in shales. Based on their observation, they used the Molecular Dynamics simulation to measure the surface tension and contact angle in nanopores. With the main results shown in Figure 2, both the surface tension and contact angle are not consistent with their scalar values, which are 475.5 mN/m and 152.5° for mercury-air-graphene interface, when the capillary radius is less than 10nm. However, the contact angle and surface tension show reverse influence on the capillary pressure value, and when both of them are considered size-dependent, these changes cause the capillary pressure to be less

in sub-10nm capillaries than obtained by the Young-Laplace equation. They argued this behavior in capillary pressure is dictated by the dramatic changes in the surface tension. Larger discrepancy is found when the capillary size is further decreased. Based on their work, it was shown that the corrected capillary pressure becomes much smaller as the capillary size is reduced below 10nm.

Recently, in a separate study, 20% discrepancy was found in the pore size distribution measurements using MICP for shale when compared with the cryogenic nitrogen adsorption method results. The discrepancy was eliminated by changing the contact angle in the Young-Laplace equation to 152.5° (Kuila and Prasad, 2013). However, the sources of inconsistency have not been identified yet.

In this thesis, a new numerical approach is presented to introduce liquid mercury into nano-scale capillaries at extremely high pressure to directly measure the nano-capillary effects on the estimated mercury-air capillary pressure values. Note that the aim of this thesis is to directly measure the capillary pressure, rather than measuring the contact angle and interfacial tension, and subsequently calculating the pressure. Due to the nature of the problem, a new molecular modeling approach is developed, where liquid mercury, capillary walls, and piston are developed atom-by-atom. We performed non-equilibrium molecular dynamics simulations of mercury intrusion into small capillary at high pressure using a piston model. The numerical results from the molecular simulations are validated using laboratory-measured density-pressure data from the literature and with the capillary pressure data for large capillaries based on the Young-Laplace equation.

CHAPTER II

MOLECULAR SIMULATION SET UP

2.1   Introduction to Molecular Dynamics Simulation

We conducted molecular dynamics (MD) simulations using Large-scale

Atomic/Molecular Massively Parallel Simulator (LAMMPS), a globally used freeware

(Plimpton, 1995). Based on the previous work in our research group, the Monte Carlo

(MC) simulation has limited success for this highly-compressed mercury study due to

massive calculation required in defining the initial equilibrium state. In this study, we

perform MD simulations for mercury bulk density computation and for mercury

capillary pressure threshold computation in nanocapillaries size from 1nm to 20nm. The

computational apparatus used in this study involves an atomistic model for a piston

which compresses liquid mercury atoms in a tank and forces them into a model capillary.

The capillary is a single-wall carbon tube with walls made of a graphene layer. The

locations of the carbon atoms that makes up the capillary is fixed and, hence, the

capillary does not deform during the simulation when it interacts with the mercury under

high pressure. Two types of atoms are used in the MD simulations: mercury and carbon.

The carbon molecules are used either to build up different sizes of nanotubes or the

piston wall to push the mercury. Initially, the geometry has been optimized and an initial

equilibrium state is defined based on the local minimum molecular potential energy in

the simulation system.

We also used Visual Molecular Dynamics (VMD), which is a freeware program

that displays the visual 3-D graphics and movement of the target atoms. It has multiple

uses and built-in functions, and in this research, it is used to visualize the movement of atoms and see whether the atoms behave properly, to check the final location of the liquid mercury atoms, and to monitor the entire progress of each simulation. VMD is also used to create different sizes of nanotubes and single layer of graphite atoms as the piston wall in the simulation, which has the length and width defined as the desired values.

In order to speed up the MD simulation, High Performance Research Computing (HPC) systems is used to do the parallel computation under the host of Ada from Texas A&M University. Each simulation takes no more than 2 hours and it is about 10-15 minutes in average. In the mercury density computation simulation, 4 cores/cpu were used; while in the mercury injection simulation, 20 cores/cpu were used. It has improved the speed of the simulation significantly comparing with running the MD simulation on a personal computer.

2.2 Force Field

Generally, the forces between two molecules are categorized as bonded and non-bonded interactions. The bonded interaction, also known as intramolecular force, is the force that holds atoms together within molecules. There are three subcategories in it, which are ionic bonding, covalent bonding and metallic bonding. The ionic bonding exists in between metals and nonmetals, the covalent bonding forms two nonmetals, and the metallic bonding actually forms within a pure metal or metal alloy. The non-bonded interaction, which is also called intermolecular force, is weaker than the intramolecular

15

force. It represents the interaction between neighboring molecules. Both the attractive and repulsive forces are found between neighboring atoms or molecules. There are four types of intermolecular forces, which are ionic force, dipole-dipole force, hydrogen bonding and van der Waals force. The ionic force, which holds ions together in ionic solids, is also known as electrostatic forces. This is the strongest intermolecular force, and it is the main interaction between charged atoms or molecules. The second type is dipole-dipole force. The dipole is defined as a molecule which has opposite charge on its two ends. For example, the interactions between H and Cl in HCl is dipole-dipole force. The third type is hydrogen bonding which is a special case of the dipole-dipole force, while the London dispersion or van der Waals force, exists between non-polar molecules. The van der Waals forces are the weakest type of all the intermolecular forces.

To be noted, there are also other ways to represent the forces among the molecules/atoms. The word "particle" can be used to represent either a single atom, a single ion, a polyatomic ion, or a molecule. Likely, when people state the "inter-particle forces", it could have different meanings, for example, ion-ion attraction, covalent bonding, polar covalent bonding, or van der Waals forces. It really depends on the circumstances that this word has been used. In this thesis, the interpartical force is referred as van der Waals force.

In the MD simulations, the bonded interaction is remained as the same for the duration of time, while the non-bonded interaction between two atoms/molecules is defined using their force field within a cut-off distance (Plimpton, 1995). In order to set
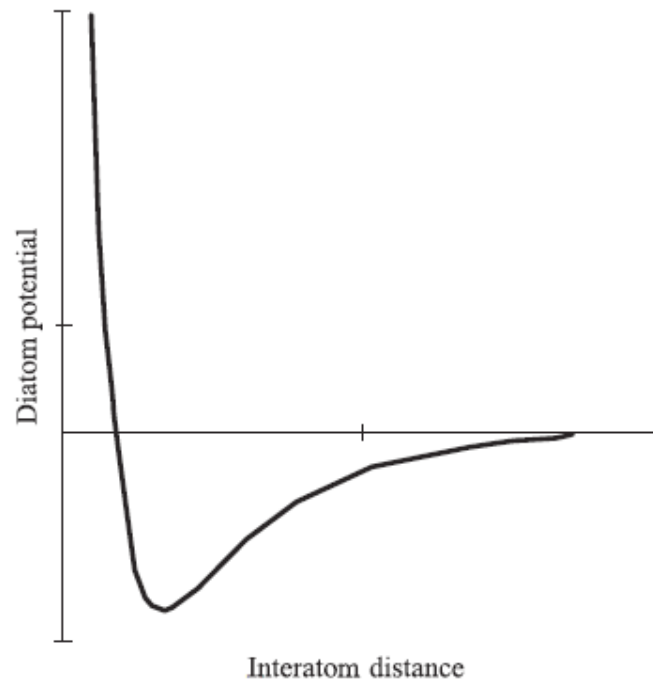
Figure 3 Mutual potential energy between two argon atoms (adapted from Hinchliffe, 2003)

up a MD simulation, the force field of each atom/molecule should be defined accordingly, so that the intermolecular forces between different atoms are properly defined and accurate, and based on that the density and energy properties of the fluid in large scale could be reproduced.

There were three groups of non-bonded interactions defined in our simulation, which were carbon-carbon interaction, mercury-mercury interaction, and mercury-carbon interaction. To be noted, there was no bonded interaction defined in our simulation, but the carbon atoms in the same layer of graphite sheet and tube were built in covalent bonding, and their location was fixed.

In MD simulation, the force field is the functional form and parameter that are used to calculate the mutual potential energy between molecules and non-bonded atoms (Hinchliffe, 2003). When one molecule/atom is moving towards the other, the typical potential energy change is shown in Figure 3. When they are separated with a large distance, the interaction in between is negligible. In order to decrease the energy, they are attracted to each other and hence getting closer, until they reach the minimum energy, and this energy in positive value is defined as the depth of the potential wall, ε. The distance between these two molecules/atoms at this point is the equilibrium distance. To further decrease their distance, additional energy should be provided, and when the potential is equal to zero, the distance at that time is defined as the collision diameter σ, also known as length scale. If the distance is continued to decrease, they become to repel each other, and this repulsive force can be much larger comparing with the attractive force. At the van der Waals radius, which is equal to half of the length scale, the two molecules/atoms reach their minimum distance.

To take a closer look, the potential contains a repulsive part, and an attractive portion when they are farer to each other. All the attractive forces fall off when the atom pair distance equals to $1/R_{AB}^6$. Usually, the repulsive term can be written as:

$$U_{repulsive} = Aexp(-BR) \tag{3}$$

where A and B are constant values depends on the type of atoms and determined based on the experiment data (Hinchliffe, 2003). As a result, the total interaction U can be simplified using the following equation:

$$U = A exp(-BR) - \frac{C}{R^6} \qquad (4)$$

where C is also varied from different atoms type and determined based on the

experiment. This equation is also known as exp-6 potential. The well-known Lennard

Jones (L-J) 12-6 potential is built based on this exp-6 potential where the repulsive term

is considered being proportional to the $1/R^{12}$, written as:

$$U = \frac{C_{12}}{R^{12}} - \frac{C_6}{R^6} \qquad (5)$$

where C_{12} and C_6 are factors determined based on the experiment. This can be also

rewrite with the well depth ε and length scale σ as:

$$U = 4\varepsilon \left(\left(\frac{\sigma}{R} \right)^{12} - \left(\frac{\sigma}{R} \right)^{6} \right) \qquad (6)$$

Usually, people use ε/k_B instead of ε when they describe the well depth, where k_B is the

well-known Boltzmann constant defined as gas constant R divided by the Avogadro

constant N_A, which equals to $1.38064853 \times 10^{-23} \, J/K$ (Hinchliffe, 2003). This

Lennard-Jones potential is more suitable when used to describe the force field of noble

gas like Argon, but when it is used in real material, it may have some limitations.

Note that finding a suitable force field for liquid mercury and validating

interaction parameters between the mercury and carbon atoms under high pressure

conditions were crucial for this work due to the special properties of mercury.

Mercury is a heavy silvery-white liquid metal at room pressure and temperature.

Atoms of metals can easily lose their outer shell electrons, which results in a free-

flowing cloud of electrons within its molecular arrangement. This provides its ability to transform heat and electricity. Mercury is relatively a poor conductor of heat but it conducts electricity well. Several attempts have been made to describe the pair potential of liquid mercury to accurately and consistently predict its properties using a thermodynamic model (Chen et al., 2005; Bomont and Bretonnet, 2006 and Iakovlev et al., 2015). The challenge was the mathematical description of the interaction between an atom and the surrounding electron cloud, in addition to the usual interactions based on van der Waals forces and electrostatic forces. In our case, there is added complexity in modeling liquid mercury due to the presence of many-body interactions and quantum effects that develops under extreme pressure. The broadly used Lennard-Jones potential simply cannot reproduce the experimental mercury data such as density, viscosity, or total energy. The electron cloud of liquid mercury is large such that the embedding potential between the mercury atoms cannot be ignored as typically done for the Lennard-Jones fluids with the dominant pair-wise interaction. We therefore choose the so-called Embedded Atom Model (EAM) as the force field in our simulation, which is often used for metals. It has previously been shown by Iakovlev et al. (2015) that using the EAM for liquid mercury gave the closest surface tension of mercury comparing with experimental data among the other density-independent or density-dependent models. The potential energy of metal such as mercury is then defined using the following equation:

$$U = \sum_i \Phi(\rho_i) + \sum_{i<j} \varphi(r_{ij}) \tag{7}$$

where the first term considers the embedding potential of each metal atom due to the many-body electronic interaction, which is basically dependent on the density of the metal, by including ρ_i, which represents the effective electron density at each position i. And the second term is the conventional Lennard-Jones potential, which represents the potential energy between each mercury atom pair. Previous work by Belashchenko (2006, 2013) provided two groups of parameterization of the EAM model for the liquid mercury. The first way defined the embedding energy using

$$\Phi = \begin{cases} a_1 + a_2(\rho_i - \rho_0)^2 + a_3(\rho_i - \rho_0)^3, \rho_i > 0.8\,\rho_0 \\ a_4\sqrt{\rho_i} + a_5\rho_i, \rho_i < 0.8\,\rho_0 \end{cases} \tag{8}$$

Because the effective electron density in different atom position is influenced by its surrounding atoms, we used the following equation to define it:

$$\rho_i = \sum_j \Psi(r_{ij}) \tag{9}$$

where

$$\Psi(r) = p_1 \exp(-p_2 r) \tag{10}$$

The parameters in these equation are adjusted according to experiment. However, to make our liquid mercury models suitable under extreme pressure (which is the condition in MICP experiment), the above parameters are not suitable anymore. As a result, we used the modified embedded atom model which was also introduced by Belashchenko (2013), and this is the other group of parameterization as mentioned before. Similarly, it defined the embedding energy but separately in each narrower range:

$$\Phi = \begin{cases} a_1 + c_1(\rho_i - \rho_0)^2, \rho_i > 0.8\,\rho_0 \\ a_k + b_k(\rho_i - \rho_{k-1}) + c_k(\rho_i - \rho_{k-1})^2, \rho_k < \rho_i < \rho_{k-1}, k = 2,3,\dots 7 \\ [a_8 + b_8(\rho_i - \rho_7) + c_8(\rho_i - \rho_7)^2] \cdot [2\dfrac{\rho_i}{\rho_7} - \left(\dfrac{\rho_i}{\rho_7}\right)^2], \rho_i \le \rho_7 \\ a_9 + b_9(\rho_i - \rho_8) + c_9(\rho_i - \rho_8)^m, \rho_8 \le \rho_i \le \rho_9 \\ a_{10} + b_{10}(\rho_i - \rho_9) + c_{10}(\rho_i - \rho_9)^n, \rho_i > \rho_9 \end{cases} \qquad (11)$$

As a result, the parameters p_1, p_2, a_1, c_1-c_{10}, ρ_1- ρ_9, m and n in equation (8-11) can be adjusted based on the experiment data of mercury. With these modifications, this model has good agreements with the mercury experimental density-energy data for pressure up to 46GPa, which is equal to 6,671,736 psi, at room temperature and for temperature up to 1,673K. This fully covers the pressure and temperature ranges for all of our simulations. The parameters we used for the mercury force field in the modified EAM model are adopted from Belashchenko (2013), where p_1=4.8019, p_2=1.3095 A^{-1}; a_1=-0.08798 eV; c_1=0.7867, c_2=-1.40, c_3=2.00, c_4=-3.00, c_5=5.42, c_6=-2.00, c_7=-3.20, c_8=4.00 eV; ρ_1=0.89, ρ_2=0.81, ρ_3=0.71, ρ_4=0.62, ρ_5=0.55, ρ_6=0.47, ρ_7=0.30. To be noted, the reason for its limitation in other condition is due to its neglect of thermal energy of electrons (Belashchenko, 2013). These factors above are used to define the mercury force field at normal pressure. When it exceeds the normal pressure, such as in our simulation, the other terms are required: ρ_8=1.20, ρ_9=2.80; c_9=0.980, c_{10}= 0.230eV; m=1.70, n=3.00. In addition, when we used this force field for mercury in our own simulation, we adopted the radius of interaction breakage as 9.01A for mercury (Belashchenko, 2006 and Belashchenko, 2013), and the cut-off distance for other

interactions in our simulation was defined as 11.01A. This is going to save the computing time because it eliminates the calculation of non-bonded interactions.

For carbon-carbon atomic interactions of the graphene walls, we used the following Lennard-Jones parameters: $\sigma_{C\text{-}C}$=3.407A and $\varepsilon_{C\text{-}C}/k_B$=28.02K. We have taken the mercury-carbon wall interaction parameters from Chen et al. (2005) where they simulated a mercury drop being added on a graphite surface and concluded that the potential well depth $\varepsilon_{Hg\text{-}C}/k_B$ is equal to 14.7K. In previous work by Wang et al. (2016), $\varepsilon_{Hg\text{-}C}$ value was modified because they believed that the contact angle was dependent on the line tension and Chen's model was only workable at 300K. Applying $\varepsilon_{Hg\text{-}C}$ suggested in Wang's paper, we tested the mercury injection simulation results. The results showed that the capillary pressure measurements were consistent with our previous simulations. Furthermore, because 298K is the temperature of MICP experiment as well as the set temperature in our simulation, the limitation due to the temperature would not influence the accuracy of our results which were measured based on the equilibrium states. The length scale between mercury and carbon was defined as $\sigma_{Hg\text{-}C}$=3.321A, which is estimated by use of Lorentz-Berthelot mixing rule and using $\sigma_{C\text{-}C}$=3.407A and $\sigma_{Hg\text{-}Hg}$=3.234A.

2.3   The Ensemble

The ensemble is also another important input in MD simulations. There are four ensembles in the theory of statistical thermodynamics. The canonical ensemble, NVT, was performed for the capillary pressure computation simulations, in which the numbers

of atoms N, the volume V, and the temperature T of the simulation remains constant.

The temperature is set to be 298K which is the room temperature and it is also the

experimental condition of MICP. Other ensemble is microcanonical ensemble, NVE,

where the energy instead of temperature are treated constant. However, because the

energy itself cannot flow from one cell to the other, thus this is a really simple ensemble;

The isothermal-isobaric ensemble, NPT, maintains the pressure constant, which was

used in our mercury force filed validation simulations, and the last one, the grand

canonical ensemble, μVT, allowed the number of atoms in each cell fluctuated. They are

used in other conditions. Further discussions in ensemble are also included in the

following parts where simulation settings are going to be introduced in details.

2.4   Bulk Density Simulation for Liquid Mercury

To begin with, the force field for mercury is validated by reproducing the mass

density of the bulk mercury at room temperature and changing pressure, and by

comparing the results with the experimental data given in Table 1. NPT ensemble was

used in these simulations. Both temperature and pressure were inputs, where the

temperature was set to be the room temperature, whereas the pressure was given a range,

which in our simulation, the upper and lower limit were both set to be the target pressure

for the density computation. To perform this simulation, 15,488 of mercury atoms were

placed inside a cubic box with the length in x, y and z direction as 9.9nm. This box was

set to be periodic in all the three directions. The periodic boundary forms the identical

box which has the atoms move out from one side of the box and return to the box from

Table 1 Experimental values of mercury density at room temperature and its dependence on pressure from (Holman and Seldam, 1994)

Pressure bars	Pressure psi	Experiment Density(kg/m^3)
0	0	13,533.6
500	7,251.9	13,560.6
1,000	14,503.8	13,587.2
1,500	21,755.7	13,613.4
2,000	29,007.6	13,639.2
2,500	36,259.5	13,664.6
3,000	43,511.4	13,689.6

Table 2 Computed bulk mercury density varying with pressure and compared to the previously published experimental data

Pressure psi	Experiment Density(kg/m^3)	Simulation Density(kg/m^3)	Difference %
12,272	13,579	13,728.9	1.1
18,260	13,600	13,749.5	1.1
20,730	13,609	13,756.9	1.1
36,994	13,665	13,801.3	1.0
45,217	13,693	13,837.2	1.1
81,657	13,809	13,951.8	1.0
122,861	13,928	14,082.3	1.1

the other side, and hence keeps N constant in the simulation box. The system is let to reach its equilibrium state at the room temperature. The density of the mercury was calculated based on the number of the atoms and the size of the box, while the pressure changes with the simulation time, hence was output from the simulation. Thus, the density-pressure relationship is concluded from this simulation.

The results and comparison with the experimental data published by Holman and Seldam (1994) are shown in Figure 4 and tabulated in Table 2. Clearly, the experimental

25

density data of mercury has been successfully reproduced using the molecular dynamics

simulations with a discrepancy around 1%. Our validation included the pressure

comparison up to about 120,000 psia, which is well beyond the limits of the MICP

apparatus pressure range. Figure 4 includes the linear regression results of the

experiment and of the simulation, which are reasonably close to each other. This

validates our simulation.

2.5   Piston Model for Mercury Intrusion into Nanocapillary

Figure 5 shows the piston model we developed to force mercury into the single-wall

carbon tube using molecular dynamics simulation. Clearly, the mercury injection setup

includes a computational box on the left filled with mercury atoms, and a carbon tube on

the right-hand side, which is connected to the mercury box. The capillary is fixed,

meaning that the carbon atoms that make up the wall are not allowed to move. Their

coordinates are built by VMD as stated in the 2.1 part. In an independent study, Feng

and Akkutlu (2015) have shown that vibrating wall atoms do not change the result of

fluid transport inside the tube significantly. The capillary diameter is set in between 1-20

nm and the capillary length is taken 3.6nm. Similar nanotube models have been used to

represent different sizes of nanopores inside the shale (Feng and Akkutlu, 2015;

Riewchotisakul and Akkutlu, 2016).

Prior to injection, the liquid mercury atoms are allowed to reach equilibrium in

the left box, Figure 5A. During this period, the mercury box has periodic boundary in all

three directions. Next, the boundary of the mercury box in z direction is changed to
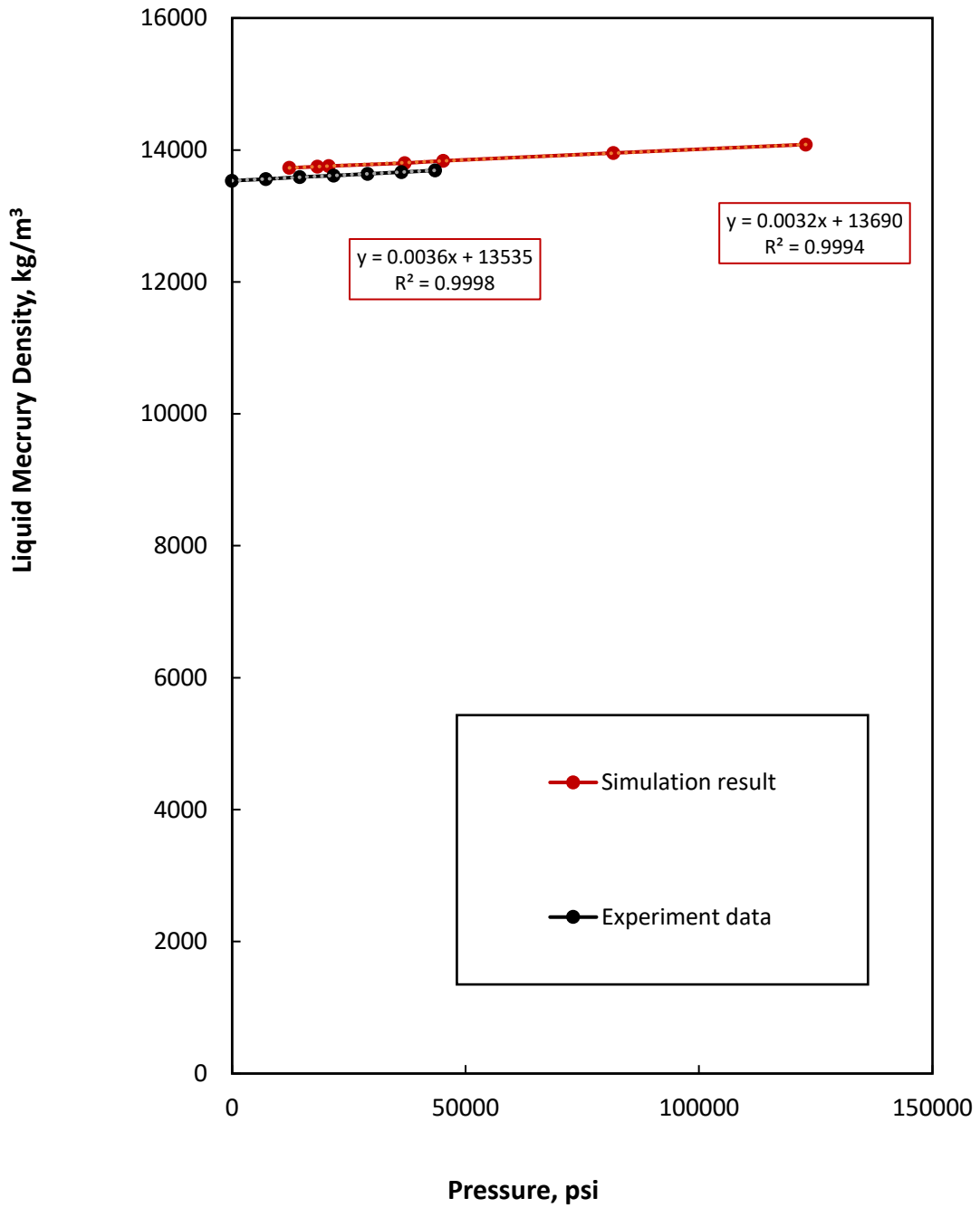
Figure 4 Comparison of the computed mercury density using molecular simulation with the experimental mercury density data from Holman and Seldam (1994)

non-periodic and shrink-wrapped, and as a result the mercury atoms can move from its original box towards the capillary tube in z direction (from the left side to the right side of the simulation box). This compressing of the mercury box is performed either by adding an external force to the piston wall or by giving a velocity to the left boundary of the mercury box. Consequently, the fluid pressure in the mercury box is gradually increased up to the intrusion pressure, Pc, when the mercury atoms are able to move into the capillary, Figure 5B, and finally filling it up Figure 5D. This is captured when piston wall is used to push the mercury atoms as in the force-based approach. While, in the density-based approach, 10% of mercury atoms intrude into the capillary tube is defined as the intrusion moment. The corresponding pressure at that moment is recorded as the capillary pressure. In this work, two different numerical methods are used to calculate the bulk fluid pressure inside the mercury tank: force-based pressure method and density-based pressure method. Detailed explanations of these methods and the computational workflow are shown in the next Chapter.

The major advantage of our mercury injection model is that the pressure inside the nanopore is in equilibrium with the bulk mercury pressure in the tank. Hence, the uncertainty and complexity of pressure calculation inside the nanopore are avoided by instead calculating the fluid pressure in the tank.
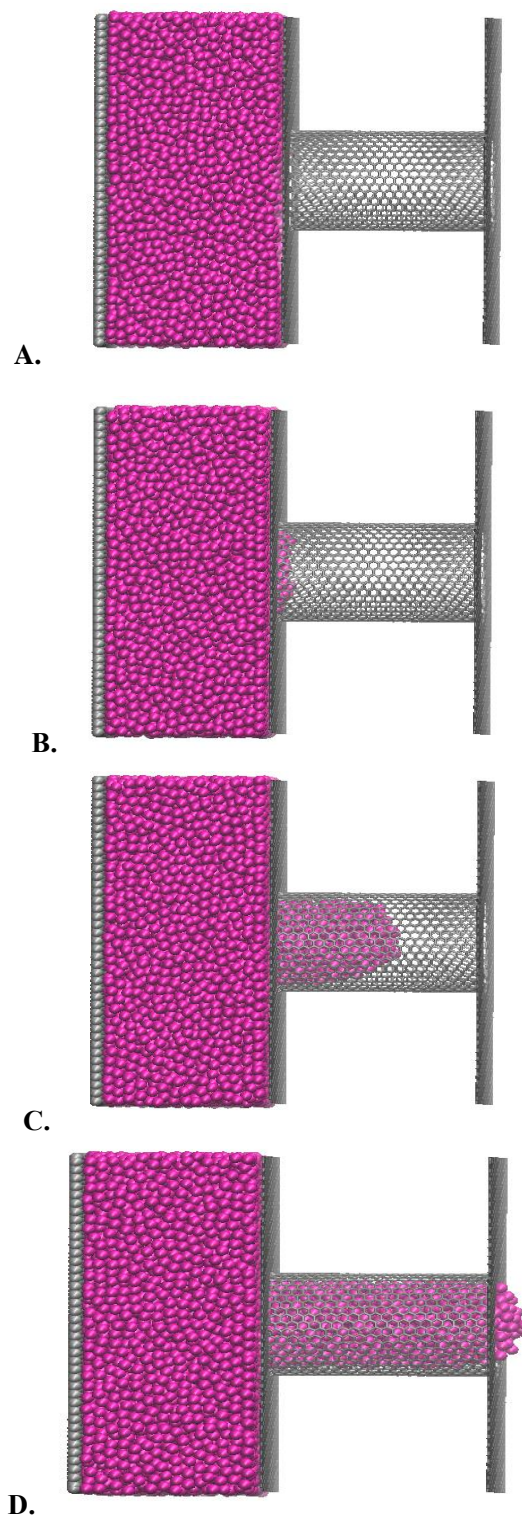
A.

B.

C.

D.

Figure 5 Molecular simulation snapshots of mercury injection into single wall carbon tube using piston at different time steps.

CHAPTER III

SIMULATION RESULTS AND DISCUSSION

The important outcome of the simulation study is the capillary pressure value which leads to mercury intrusion. Below, two computational methods are presented to predict the pressure: forced-based and density-based methods. Following, a rigorous discussion on the applicability of the Young-Laplace equation to displacement in nano-scale capillaries is presented.

3.1 Force-based Pressure Approach

In this approach, a layer of graphene was used to mimic the piston as shown in Figure 6. The dimension is the same as the mercury simulation box. The interaction between the graphene layer and mercury atoms was defined using the mercury-carbon interaction parameters as stated in Chapter II.

Initially, the system is let to reach its thermodynamic equilibrium. This happens during the simulation, when the total energy of the system reaches a minimum level and stays at that level. In order to compress the mercury in the tank, a constant and uniform external force was applied on the carbon atoms that make up the piston. In this way, the structure of the wall did not change during the push. The applied external force on the atoms of the piston was the averaged desired force, as a result, each graphene atom received the same desired force. Hence, the movement of the piston was controlled by that force. Accordingly, the total force F on the cross sectional area of the piston is calculated as:

$$F = f * N_{wall} \tag{12}$$

where, f is the applied external force each carbon atom perceives, and N_{wall} is the total number of carbon atoms that make up the piston wall. Hence, the external pressure on the mercury tank is:

$$P = \frac{F}{A} \tag{13}$$

where A is the area of the piston.

In each simulation, a particular level of constant force is applied to observe whether the mercury intrude into the capillary at this particular force or not. The pressure at the minimum force for the mercury intrusion is the capillary pressure at this tube size. After we observe the intrusion, we let the simulation continue for longer time and check whether the mercury atoms would continue penetrating into the capillary and
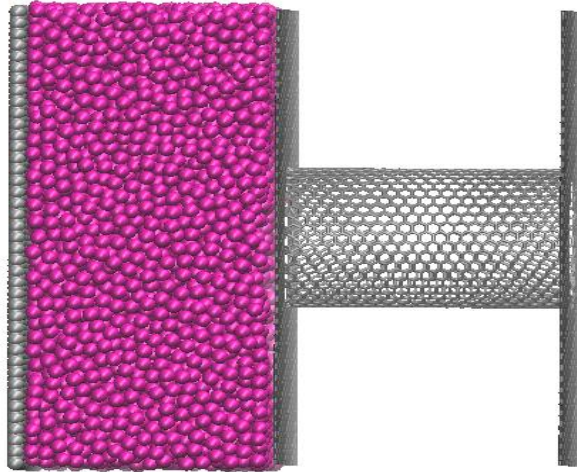

Figure 6 Illustration of mercury injecting to nanocapillary using force-based measurement for the fluid pressure in the tank. A moving wall which is made of graphene is introduced to the left side of the mercury tank to push it into the pore.
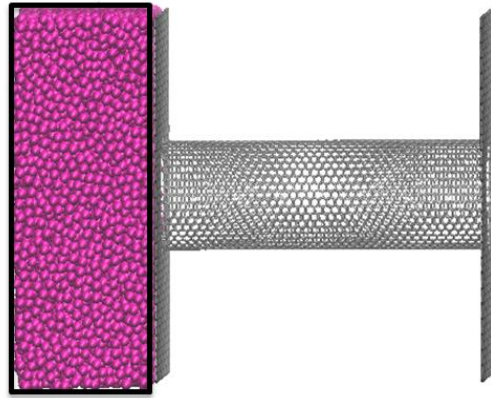
31

Figure 7 Illustration of mercury injecting to graphene capillary using density-based measurement for pressure. During the simulation, the left boundary of the simulation box moves to the right which results in compressing the mercury slab and force it into the pore.

finally fill up the entire capillary tube under this external pressure. If the answer is

positive, that pressure P is recorded as the capillary pressure P_c at this size.

3.2   Density-based Pressure Approach

In this method, the system is also allowed to reach to its initial equilibrium as in

the force-based case. The graphene layer (i.e., piston) was removed in this method

because in this way the wall effect was eliminated comparing with the force-based

method. The compression of mercury in the tank was achieved by changing the volume

of the mercury tank. As shown in Figure 7, the left boundary is now set to move towards

the capillary tube in a constant velocity 0.2 A/picosecond. As a result, the pressure inside

the mercury tank increases at a somewhat constant rate. We monitored the location of

the mercury atoms, and when the intrusion is found in the capillary tube, we freeze the

location of the left boundary and maintained the volume of mercury tank constant. To
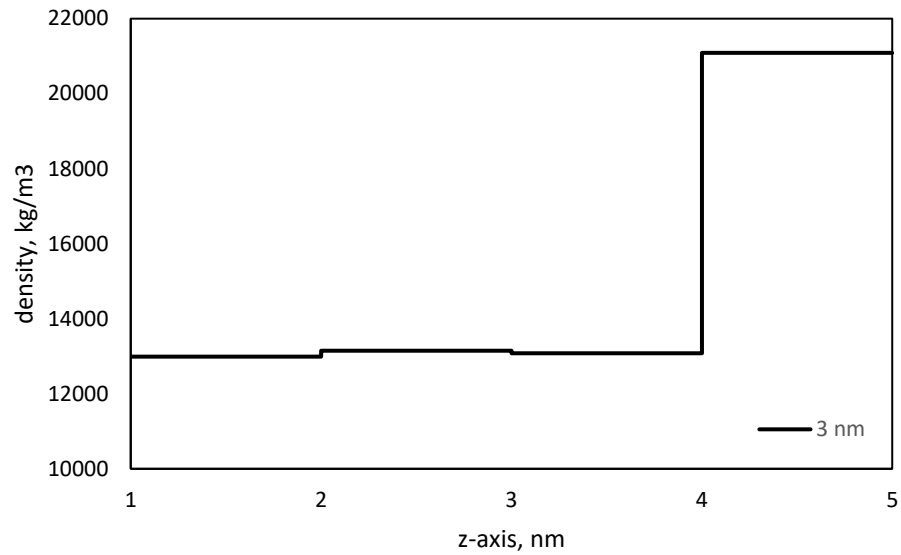
Figure 8 Local density profile in the mercury box. The left boundary of mercury tank is z=0 and the right boundary z=5nm, where it connected to the capillary tube.

better capture the location of the mercury atoms, the number of mercury atoms inside the capillary tube is counted at every time step throughout the simulation. At the early stage of the compression, the number of mercury atoms in the capillary tube is zero. When 10% of the mercury atoms were found inside the capillary tube, we assumed that the mercury intrusion occurred at that time step and freeze the location of the boundary at that time to do further computation for that state.

Afterwards, we let the mercury inside the tank to reach the equilibrium state again. We checked the final location of the mercury atoms inside the capillary and counted whether there were still 10% in there. If the answer is positive, the pressure now inside the mercury box is the capillary pressure for that tube size. LAMMPS does not directly give the value of this pressure as output under the NVT ensemble; hence we should calculate the pressure value and, for this purpose, the density of the mercury in

the tank is used. The number of mercury atoms inside the tank is counted, and the

density of mercury is calculated based on:

$$\rho = \frac{m}{V} = \frac{nM}{V} = \frac{N}{N_A} \cdot \frac{M}{V} \qquad (14)$$

where ρ is the density, m the mass, V the volume, n the number of moles, M the

molecular weight of mercury, N the atom number, N_A the Avogadro's number. Because

the number of mercury atoms can be counted, the density of the mercury is calculated

precisely based on equation above. Note, however, that the density inside the mercury

box is not constant across the width of the tank as we can see in Figure 8. Apparently,

the density is highest at a distance 4-5nm away from the capillary entrance, where the

adsorption layer develops by the capillary. After the mercury intrusion into the capillary,

the location of the left boundary is always in between 0-1nm in z axis. As a result, the

average number of the mercury atoms in 1-4nm region is used for the density

calculation. Finally, the pressure at that density is calculated using the laboratory-

measured density-pressure data phase diagram from Holman and Seldam (1994).

3.3   Comparison and Discussion of Two Approaches

The simulation results for each capillary size are plotted in Figure 9 using both

density-based and force-based pressure data. As we can see in the plot, the simulation

data using both approaches agree well with the Young-Laplace equation for the

capillaries with diameters larger than 15nm, which further validates the simulation

setting of mercury-air capillary pressure computation. The computed capillary pressure

based on two approaches also agree with each other in reasonable range. However, note that, when the capillary size is reduced to 10nm and below, the capillary pressure shows discrepancy between the simulation and the Young-Laplace equation. This agrees with the previous work by Wang et al.(2016), which also indicates that the accuracy of using the original Young-Laplace equation on capillary pressure computation is limited in this range. The simulation results are consistently higher than the values estimated from the classical theory. We believe that the enhanced capillary pressure is due to the increasing effect of the local tangential pressure in nanopores. Further on this discussion is in the next part.

As shown in Table 3, however, we observe discrepancy in nanocapillaries with diameter in between 1-10nm in the estimated P_c values using the two computational methods. We hold the opinion that the simulation results of the force-based method are more reliable for these small capillaries and the reason for this bias can be explained in three points as follows. Firstly, there is difference in the piston wall movement. In the force-based approach, each graphene atom of the piston wall is applied the same force, hence all of them are moving towards the capillary tube in a constant and uniform velocity, additionally pushing the mercury atoms ahead to the capillary tube. In contrast, the density-based approach is moving the left boundary of the mercury box in a predefined velocity. In the latter case, due to the extreme repulsive forces from the mercury atoms, the boundary movement is relatively unstable with a negative acceleration. As a result, using a piston with an applied force is a more stable way to mimic the mercury injection process. Secondly, the intrusion pressure predicted with the

Table 3 Comparison of the simulation results with Young-Laplace equation.

Capillary tube diameter	Pc, Young-Laplace equation	Density-based Pressure	Percentage Error	Force-based Pressure	Percentage Error
[nm]	[psi]	[psi]	[%]	[psi]	[%]
1.0	244,692.8	312385.5	27.7	410,610.9	67.8
2.0	122,346.4	195287.9	59.6	195,287.9	59.6
3.0	81,564.3	164440.0	101.6	149,313.1	83.1
4.0	61,173.2	120433.2	96.9	88,654.6	44.9
5.0	48,938.6	67215.7	37.3	57,858.8	18.2
10.0	24,469.3	31758.4	29.8	23,727.6	3.0
15.0	16,312.9	15226.2	6.7	16,333.6	0.1
20.0	12,234.6	12223.4	0.1	12,223.4	0.1

density-based computation may exceed the true capillary pressure value. The velocity of moving the left boundary is limited to a minimum 0.2A/picosecond (or 20m/s), and the trajectories of the mercury atoms are recorded every 0.5ps interval. As a result, the earliest intrusion moment which may appear at a particular time gap could be missed. By using the force-based approach, however, we can eliminate this limitation because the force applied on the mercury atoms was modified accurately in four decimal places; hence the changes in external pressure are really flexible and its accuracy of the capillary pressure is far better guaranteed. Thirdly, in the force-based approach, the complete filling of mercury inside the capillary tube is more reliable as defining an intrusion moment rather than just seeing 10% of the mercury atoms being forced into the capillary tube in the density-based approach. Therefore, in the following analysis, the force-based capillary pressure data is used. Furthermore, we note that the effect becomes more and more significant as the capillary size is decreased. Previous work also showed similar
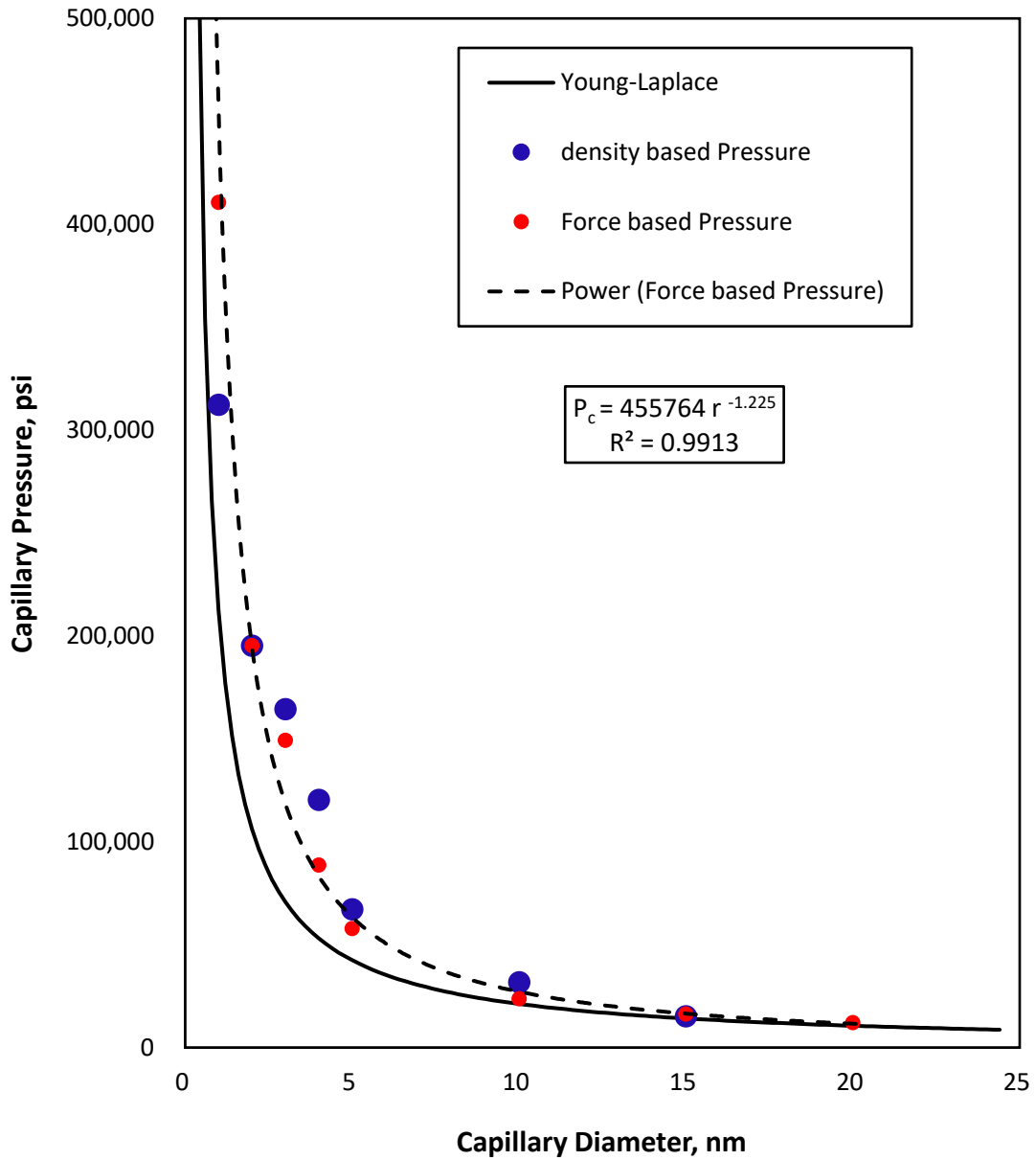
Figure 9 Comparison of the computed capillary pressure with the Young-Laplace equation

results that the surface tension and contact angle differed larger from their scalar values as the capillary size became smaller and smaller in sub-10nm range.
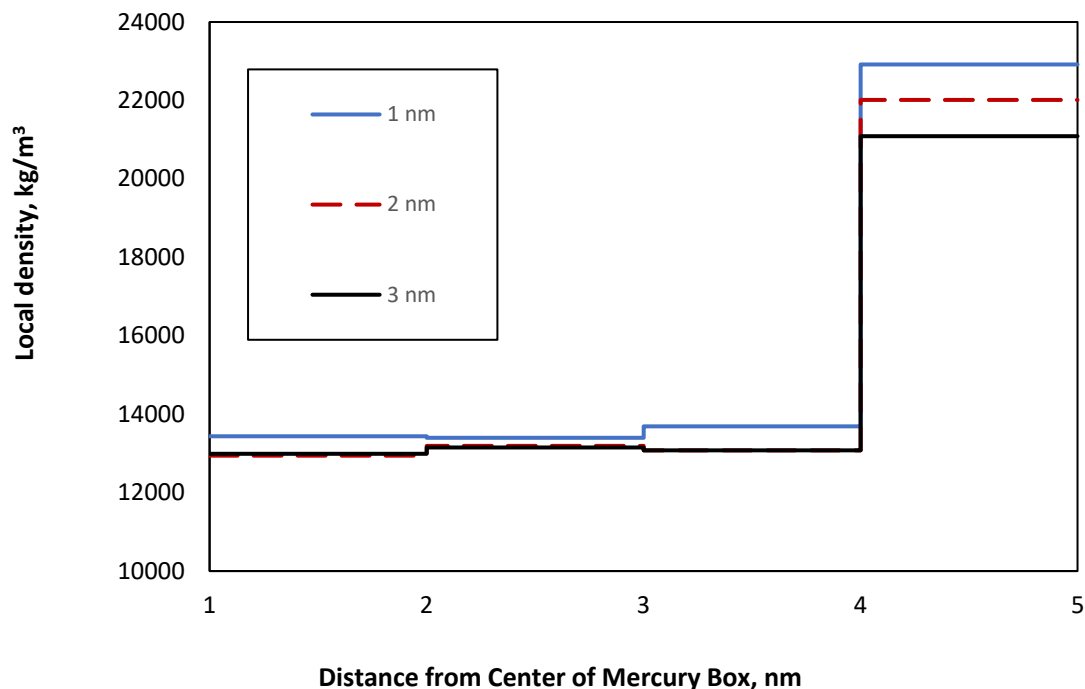
Figure 10 Comparison of local density inside the mercury box in different capillary sizes' simulations from density-based pressure measurement. The capillary tube is connected to the mercury box at 5nm.

3.4   Deviation in Capillary Pressure in Nanopores

Mercury inside the nanocapillary exists in two thermodynamic states: as the adsorbed phase by the capillary wall and as free fluid at the central portion of the capillary, if the capillary is large enough. As mentioned in chapter I, the Young-Laplace equation only accounts for the average pressure which is valid at the macroscopic scale. Mercury molecules in the adsorbed phase become the majority inside the nanocapillary and the high tangential pressure in the adsorbed phase increases the capillary pressure (Bui and Akkutlu, 2015). In our simulations where the density-based pressure values were computed, we found that the adsorption layer at the entrance of the nanocapillary

where the local high density is captured, and it also contributed more as the capillary

size was decreased shown in Figure 10. As a result, the capillary pressure in the sub-

10nm nanopores should also expected to be higher than the Young-Laplace equation

values. In addition, as the capillary size decreases further, the discrepancy should also

become much larger due to the higher and higher contribution of the adsorbed layer, and

this effect is also captured in our simulation as shown in Table 3. Note that for a 1nm

capillary the simulation gives capillary pressure that is 68% larger.

3.5 Correction to Young-Laplace Equation

Based on the results and discussion, the following power-law modification to the

Young-Laplace equation can be proposed in order to capture the nanocapillary effects

observed in the simulation study:

$$P_c = \frac{2\gamma cos\theta}{r} * G(R) \tag{15}$$

where G is a correction factor for the capillary pressure, which is a function of

normalized radius R. We define the normalized radius as $R=r/\sigma_{(Hg-C)}$. Here, σ_{Hg-C} is the

mercury-carbon length scale, which is equal to 3.321A, as stated earlier in the

Methodology section. Correction factor G and its dependence on the radius R can be

described as follows:

$$G(R) = R^{aR^b} \tag{16}$$

This equation above shows that the correction factor G has this double power

dependence to the normalized radius R. Based on the computed capillary pressure vs.

capillary radius plot shown in Figure 9, it is power-law relationship between these two

parameters. Note the nonlinear dependence of the correction factor to the capillary radius

is shown in Figure 9 which is clearly indicating that the correction is major for the

nanocapillaries with diameter below 10nm. When applying the force-based pressure data

in Figure 9 as the target, the nonlinear regression gives the constant parameters in

equation (16) as a=2.213 and b=-1.37 and the relative coefficient of determination of the

curve-fit is 0.975. This value indicates that the corrected Young-Laplace equation agrees

well with the computed capillary pressure from our simulation. In Figure 11 we plot the

correction factor G as a function of the normalized capillary radius R using the values of

the constants a and b. Based on the results, the modified Young-Laplace equation can be

re-written as follows:

$$P_c = \frac{2\gamma cos\theta}{r} * \left(\frac{r}{\sigma_{Hg-C}}\right)^{2.213\left(\frac{r}{\sigma_{Hg-C}}\right)^{-1.37}} \quad (17)$$

Note that the discrepancy between the estimated pressure values is not constant, and it

increases as we further decrease the capillary size. Based on these observations, we

believe the correction should be also carried out using a power law equation, and the

corrected portion should also be a power-law dependent function of the capillary radius.

In order to keep the original unit for the capillary pressure and make the corrected Pc

meaningful, we used the normalized radius R which defined the correction factor G also

a unit less function. If we define this dimensionless R by dividing the capillary radius
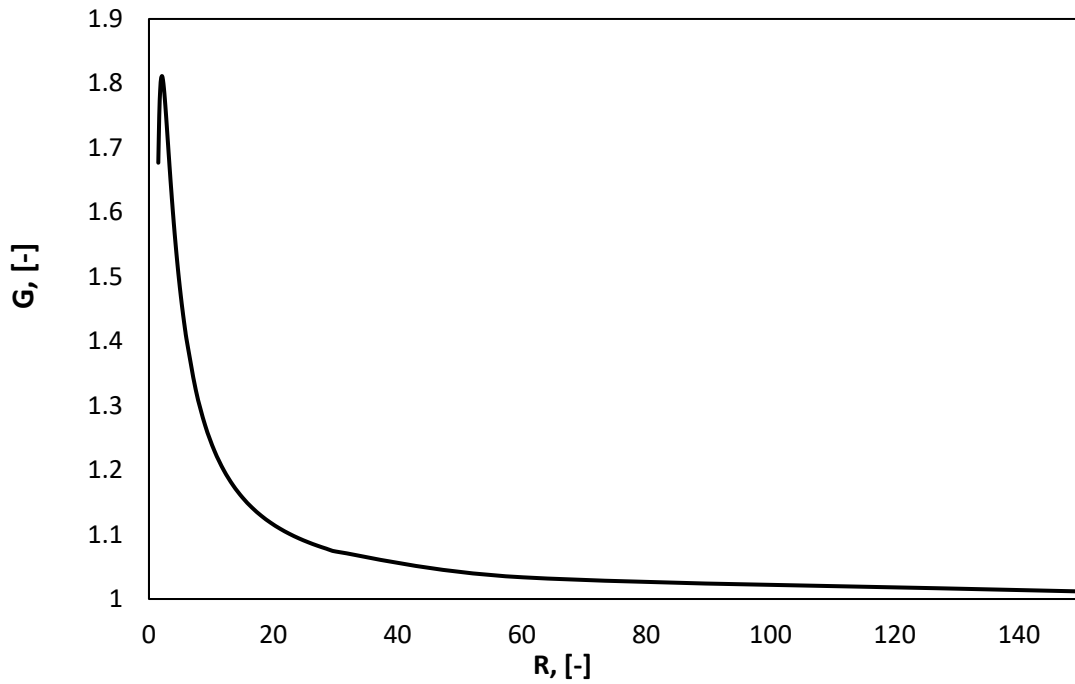
Figure 11 The relationship between the correction factor G(R) vs. normalized capillary radius R.

with a different parameter in length dimension, the functional form of this correction

will not change. Only constant factors *a* and *b* will become different. The other

requirement of the correction is that the asymptote of the correction term should be equal

to 1 in order to have the consistent prediction for the capillary pressure. This means that

the corrected capillary pressure should agree with the original Young-Laplace equation

value in larger size capillaries because the original equation is still valid when the

capillary radius is larger than 20nm.

Figure 12 shows the quality of the curve-fitting based on equation (17). We note

that the modified equation not only corrects the capillary pressure at small capillaries but
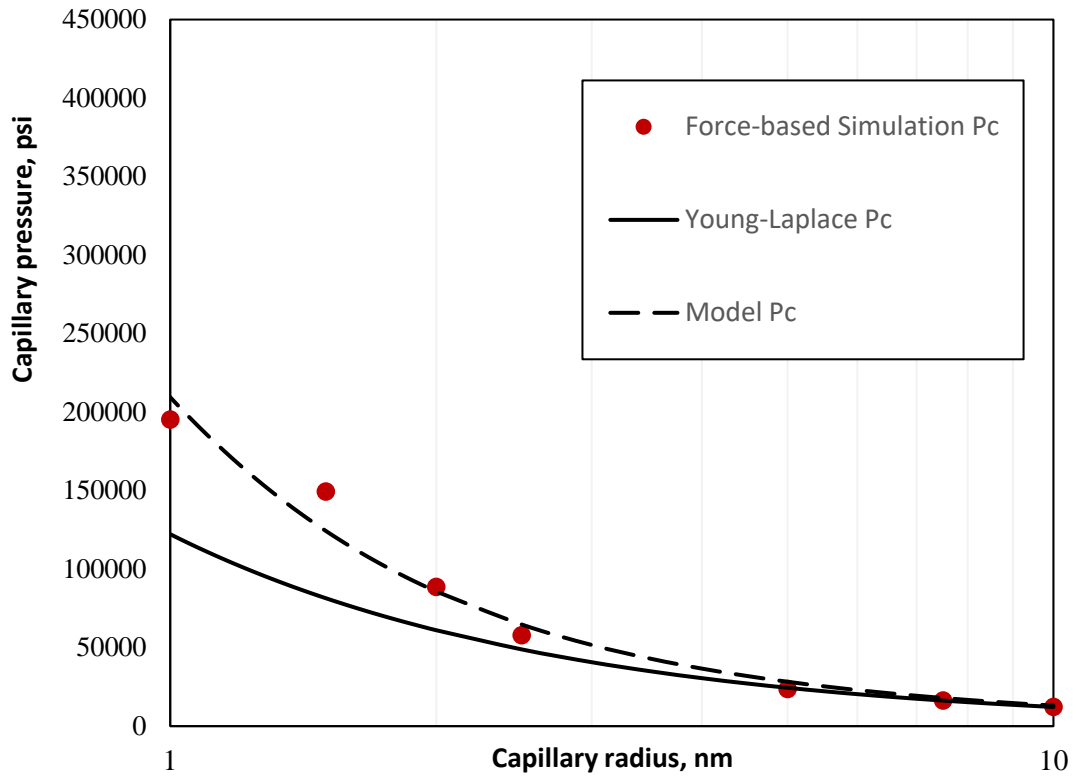
Figure 12 Comparison of the Young-Laplace equation and the Modified-Young-Laplace equation at capillary radius below 10nm.

also recovers the values associated with the large capillaries. This indicates that the correction function G goes to unity in the large capillary radius limit. This is shown in Figure 13 for capillary radius up to 200 nm. Notice that there is a peak value for G when the normalized radius is equal to 2.075. To figure out the reason of this peak, the derivative of equation (17) is taken equal to zero:

$$\frac{dG(R)}{dR} = R^{\frac{2.213}{R^{1.37}} - 2.37}[2.213 - 3.03181\ln(R)] \qquad (18)$$
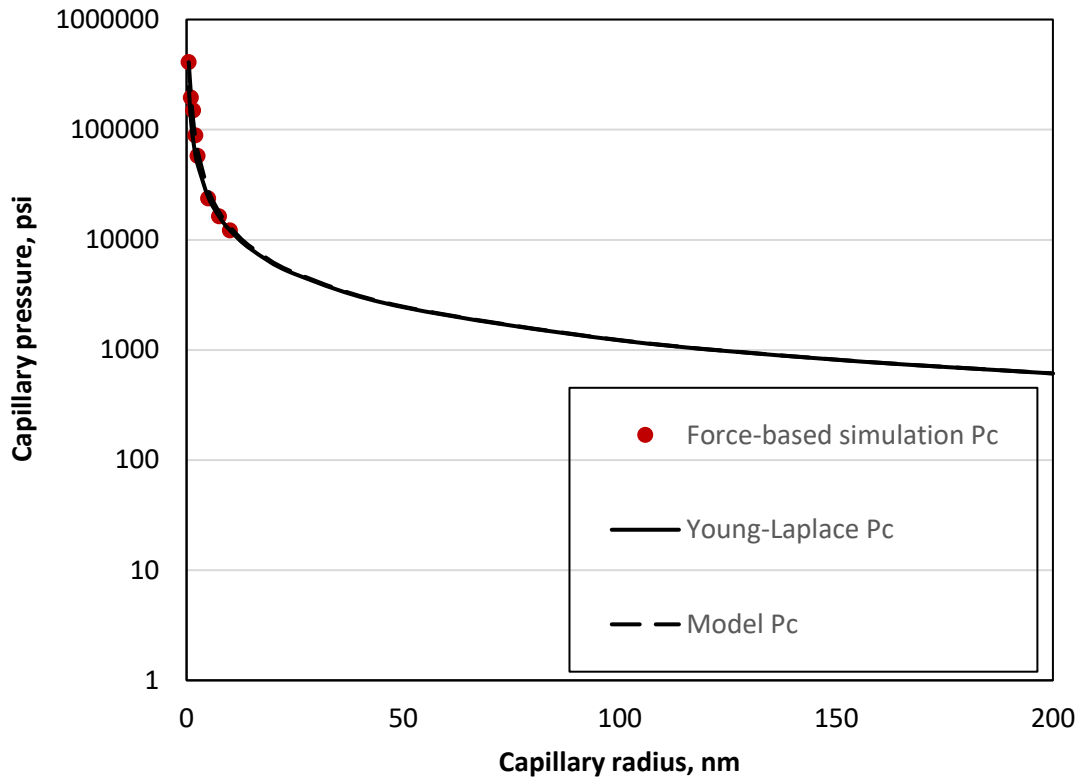
Figure 13 Comparison of the Young-Laplace equation and the new model prediction for Pc at radius up to 200nm

As we can see in this equation above, only when the term $2.213 - 3.03181\ln(R)$ is equal to 0we will have the maximum value of G. This gives R=2.075. At this point the capillary radius is:

$$r = 2.075 * \sigma_{Hg-C} = 0.0666nm = 0.6A \qquad (19)$$

Since this value is too small for the MICP measurements we decided not to worry about the maximum point in G function.

To be noted, at capillary radius equal to 10nm and 15nm, the relative error between the modified Young-Laplace equation and the original Young-Laplace equation is only 7.33% and 4.64%, respectively. For mercury-air capillary data inside graphene nanopores, we therefore believe that the nanopore correction using equation (17) is only needed for the capillary radius less than 10nm.

CHAPTER IV

APPLICATION

4.1   Correction to MICP Measurement using Shale Samples

To explore the influence of capillary pressure correction on the pore size distribution and total pore volume measurements using MICP, we compared our model results with the common analysis for the MICP data of four selected organic-rich shale samples shown in Figure 14. The selected samples with the MICP data are from shale gas basins in North America. For further clarity, we are using equations (1) and (17), with contact angle of 140° and surface tension of 480mN/m, which are the values commonly used in the industry. Clearly, the modified Young-Laplace equation has perfect match with pore diameter larger than 20 nm. When the pore size decreases, however, the discrepancy between the original and the corrected models appears, mainly below 10 nm.

As explained in the Introduction, the incremental pore volume is measured in small pressure increments up to 60,000psi for all the samples. The corrected model indicates that at the maximum injection pressure of 60,000psi, the corresponding pore throat diameter is now estimated 4.77nm instead of 3.6nm. As a result, the error in the theoretical value of the capillary pressure is 33.6% for the lowest measured pore size. One would argue that the discrepancy maybe even larger because of the compressibility of the shale rock. It is noticed that at the highest injection pressure of 60,000 psi, for a $1cm^3$ sample, it could be compressed up to $0.06 \ cm^3$ (Giesche, 2006) which is 6% volume change in total pore volume of a core sample. Because of that, the actual

45

Table 4 Comparison between the original and corrected MICP on the total pore volume measurement for shale

	Predicted cumulative pore volume and error			
Sample #	A	B	C	D
MICP (mL/g)	0.007509	0.003136	0.005207	0.006887
Corrected MICP (mL/g)	0.009210	0.004296	0.006472	0.007735
Relative Error	18.82%	19.86%	16.14%	14.02%

pore size distribution maybe shifted even further to the right due to this compressibility effect. The compressibility effect could have a stronger impact as the pore size decreases. The compressibility effect also develops for the liquid mercury in the sample cell. In addition, as observed in this study, the classical Young-Laplace equation results in an under-estimation of the total pore volume of the samples. The compressibility effects will be investigated in another study.

The impact of the proposed correction to the measurements of the cumulative pore volume is shown in Figure 15 for four shale samples A-D. The original Young-Laplace equation underestimates the shale total pore volume for up to 20% based on the 4 samples we tested. The errors associated with the total pore volume measurements are summarized in Table 4 for the samples.

An example calculation of total pore volume correction is shown here for sample A, while for other samples, similar corrections have been done and tabulated in Table 4. In the cumulative pore volume plots, at the corrected lower end of the MICP measurements, which now corresponds to 4.8 nm, we have the original measured total pore volume for shale sample A as 0.01566 mL/g. While the corrected total pore volume

is 0.0186 mL/g. Based on the difference, the error in sample A's total pore volume

estimation can be calculated as:

$$\frac{0.0186 - 0.01566}{0.01566} \times 100\% = 18.82\% \tag{25}$$

4.2   Discussion on Other Multi-phase Flow Studies

The modified Young-Laplace equation is able to correct the MICP measurements

for a more accurate pore size distribution. It brings up the interests on studying other

fluid displacement systems, such as water displacing oil, and it also has potential

application in understanding the multi-phase flow behavior of other nanoporous material

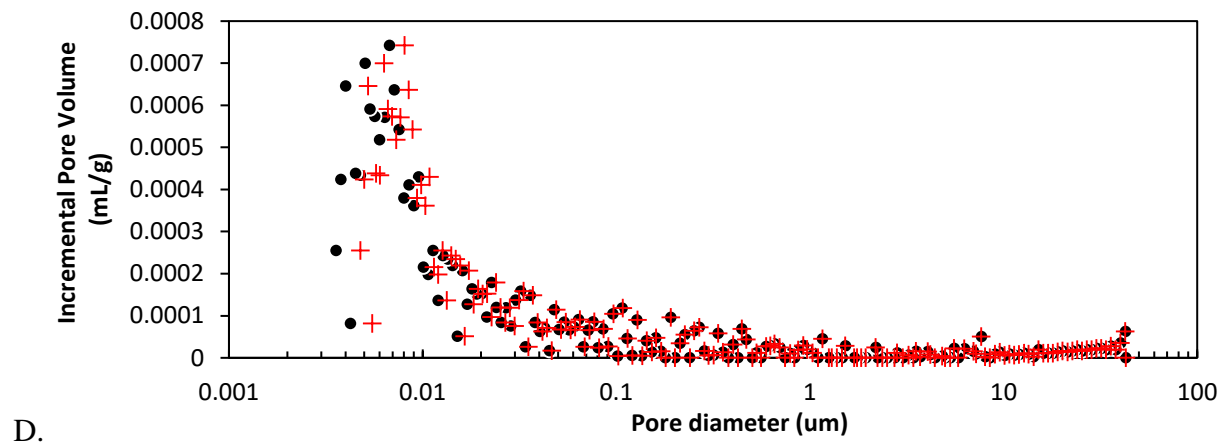using MICP. The increase in the total pore volume comes from the shale nanopores.
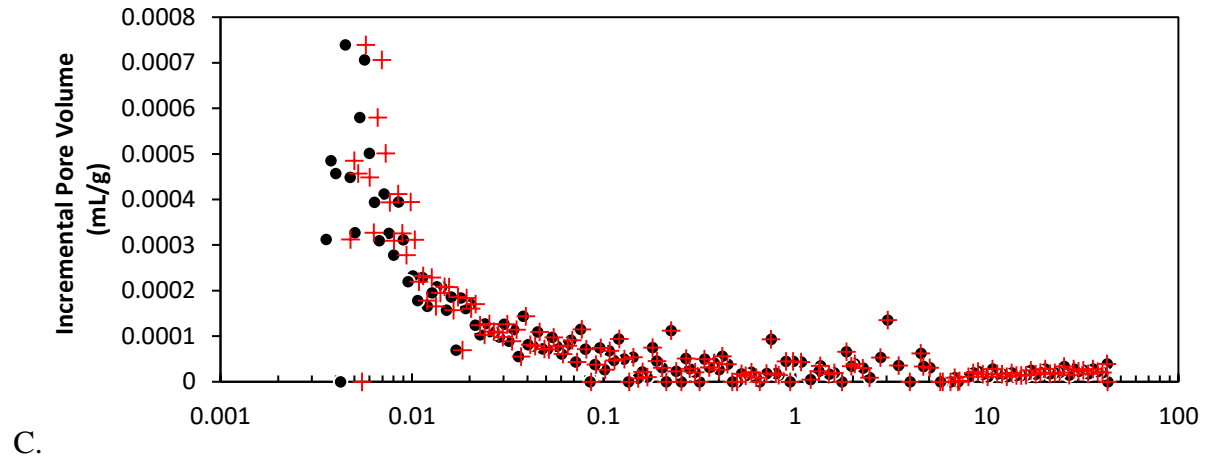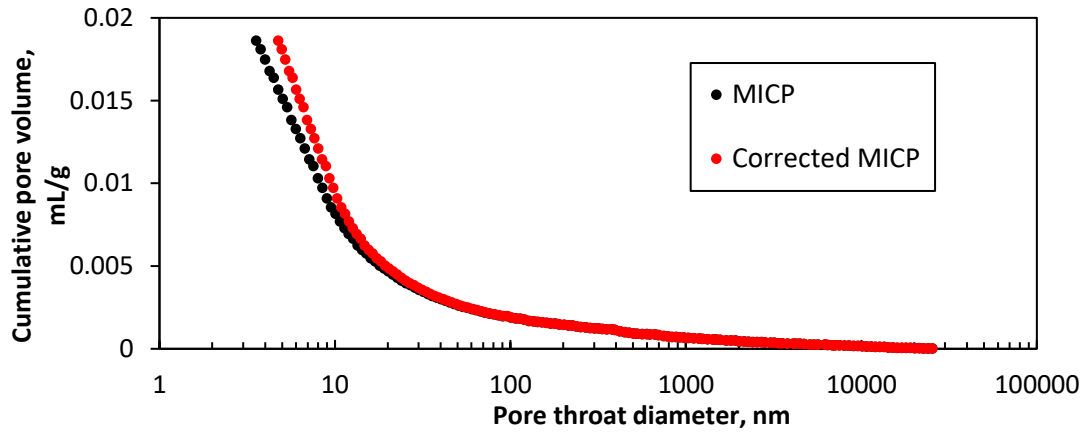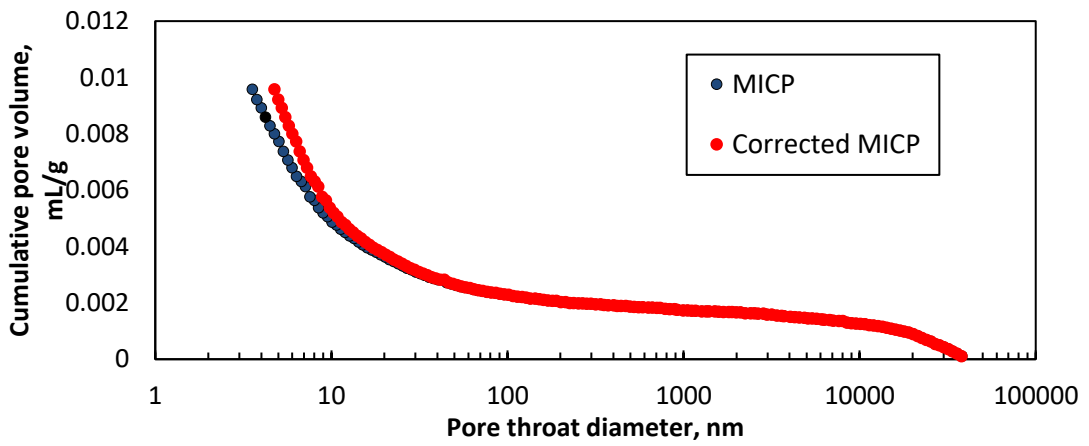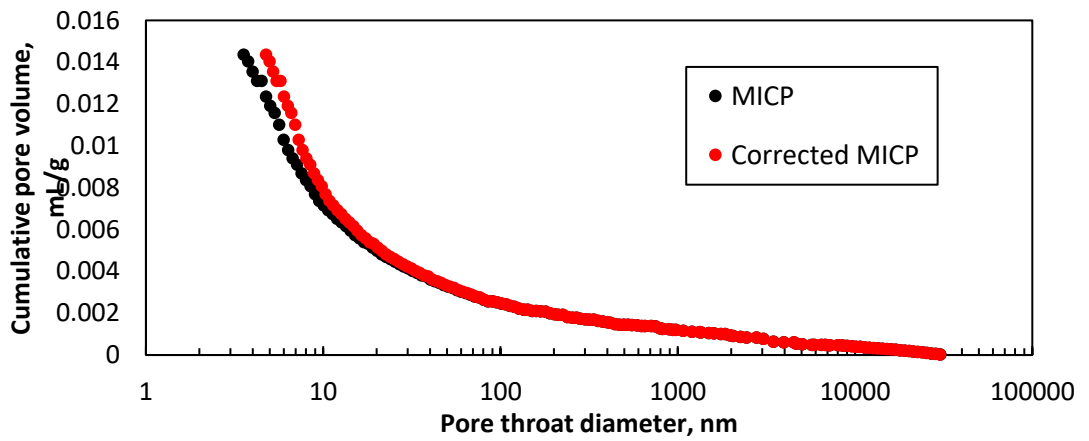
A.

B.

C.

D.
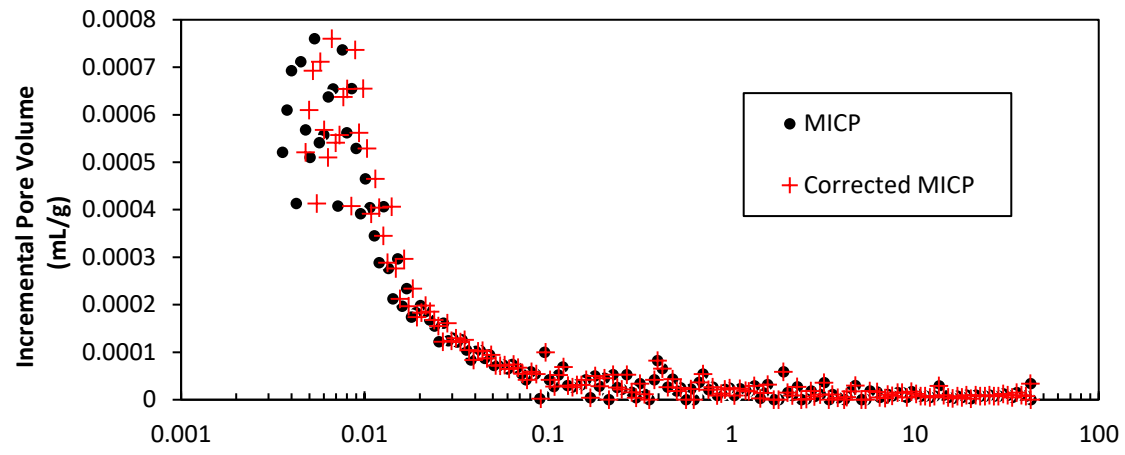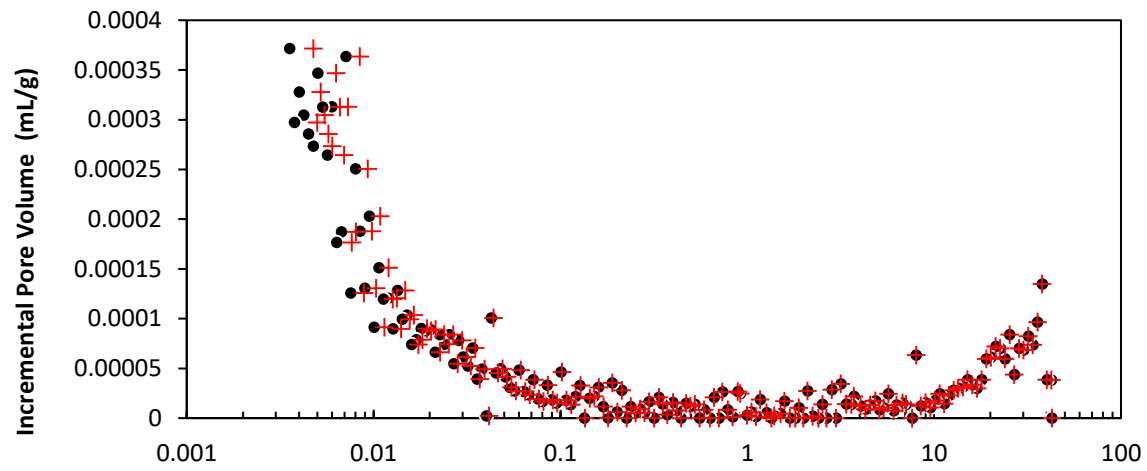
Figure 14 MICP data for samples A, B, C, D. The results are shown using the Young-Laplace equation and the modified Young-Laplace equation.
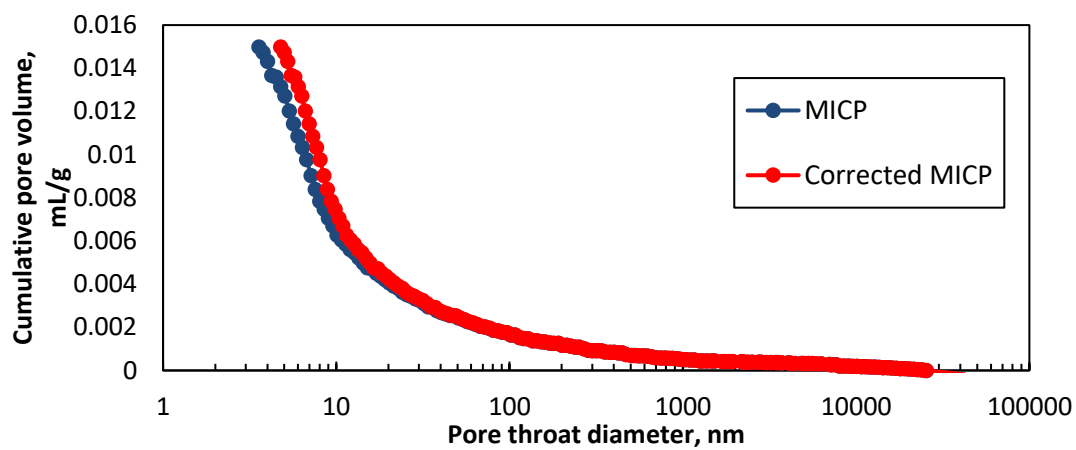
A.

B.

C.

D.

Figure 15 Predicted cumulative pore volume for Sample A-D as a function of pore diameter using MICP.

CHAPTER V

CONCLUSION

5.1 Summary

Resource shale is rich in nanopores. A significant portion of nanopores in shale is less than 10nm. It is important to better understand the pore size distribution and pore throat distribution of shale in order to have a deeper understanding of the fluid flow and transport in shale formation. The MICP experiment, as the most traditional way to measure the pore size distribution, has the largest range of measured pore size distribution comparing with the other approaches, and it costs less time and effort. The MICP experiment provides the injection volume as the pressure is increased in steps, and the Young-Laplace equation provides the basic theory to relate this injection pressure to the size of pores. However, recent study found that both the contact angle and surface tension in the Young-Laplace equation behave differently comparing with common knowledge and they become strongly size-dependent at sub-10 nm range. In this work, the molecular dynamics simulation is used to revisit the capillary pressure in nanopores, with the size varied from 1nm to 20nm, and a correction to the Young-Laplace equation is proposed to increase accuracy of the MICP experiments. Using molecular dynamics simulation, we overcome the current limitation of the experimental pressure, and measured the capillary pressure in extremely small range. We applied the corrected Young-Laplace equation to shale samples pore size distribution measurement, and captured as high as 20% error in the total volume predicted. This really matters for accurate shale pore size distribution measurement.

Our simulation has been validated by testing the accuracy of the way we describe the atomic behavior using embedded force field with the experimental energy and density results. In addition, good agreement in between the simulation and experimental results using Young-Laplace equation in large pores further validated the piston developed. Good matches are also found when the corrected Young-Laplace equation is applied in the MICP experiment comparing with the original results in large pores. The proposed correction function consistently predicts the capillary pressure from a very small pore such as 1nm diameter to macropores with sizes larger than 50 nm.

5.2 Conclusion

Using molecular dynamics simulations, it is shown that the widely-known and used Young-Laplace equation gives errors in capillary pressure estimation up to 70% in the presence of nanocapillaries. Relatively, the MICP experiment only measured the total pore volume in the lower size range as 4.8nm instead of 3.6nm, resulting the underestimate in shale total pore volume. In turn, the estimated total pore volume is expected to be in error up to 20%, based on the measurements with four shale samples. We propose a power-low correction to the equation. It is quite interesting to observe such a large error due to small pore correction to the Young-Laplace equation. Our results are therefore important for the pore size distribution measurements of nanoporous shale formations using MICP and indicate the need for further research in our understanding of multi-phase flow behavior in nanocapillaries.

5.3 Recommendation for Future Work

Future work can be continued to compare our corrected Young-Laplace equation for Pc calculation with experiment data for capillary pressure in sub-20nm range. In addition, a separate investigation is recommended to study compressibility effect on the pore size distribution and on the pore volume. This could be done by injecting the mercury into parallel tubes where multiple tubes in same size is used for capillary pressure computation in MD simulation. An example of the capillary tube structure is shown in Figure 16. By doing this, the mercury would have enough time to squeeze into the pore at extreme pressure comparing with the case where only one single tube was used to compute the capillary pressure. Reasonable agreed results should be expected from this future study when compared with the capillary pressure results in this thesis.

In addition, MICP experiments with materials like monodispersed silica spheres and Vycor glass samples can be used to measure the capillary pressure at different sizes. This can further test and validate our correction to the Young-Laplace equation.
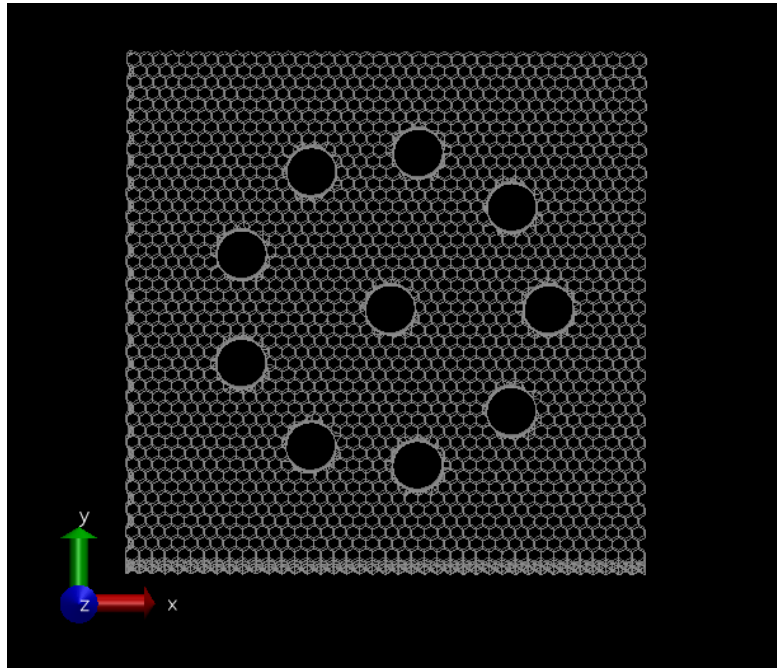
A.
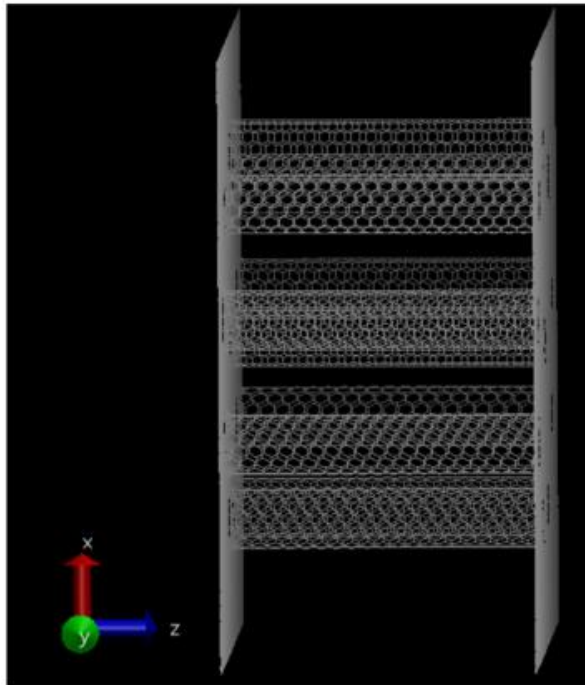
B.

Figure 16 Parallel tube structure

REFERENCES

Abell, A.B., Willis, K.L., and Lange, D.A. (1999). Mercury Intrusion Porosimetry and Image Analysis of Cement-based Materials, J Colloid Interface Sci, 211(1): 39-44. doi: 10.1006/jcis.1998.5986

Adesida, A.G., Akkutlu, I.Y., Resasco, D.E., and Shekhar Rai, C. (2011). Characterization of Barnett Shale Kerogen Pore Size Distribution using DFT Analysis and Grand Canonical Monte Carlo Simulations. SPE-147397-MS presented at SPE Annual Technical Conference and Exhibition in Denver, Corlorado; October 30-November 2

Akkutlu, I.Y., and Fathi, E. (2012). Multiscale Gas Transport in Shales with Local Kerogen Heterogeneities. SPE Journal, 17 (4): 1002-1011. doi: 10.2118/146422-PA

Apisaksirikul, S. (2016). The Development and Application of a New Semi-Analytical Model to Estimate Permeability from Mercury Injection Capillary Pressure. Master's thesis, Texas A&M University. Available electronically from http://hdl.handle.net/1969.1/157141

Awasthi, A., Bhatt, Y. J., and Garg, S. P. (1996). Measurement of Contact Angle in Systems Involving Liquid Metals. Meas. Sci. Technol, 7 (5): 753-757

Belashchenko, D.K. (2006). Application of the Embedded Atom Model to Liquid Metals: Liquid Mercury, High Temp 44 (5) 682-692. doi: 10.1007/s10740-006-0082-3

Belashchenko, D.K. (2013). Application of the Embedded Atom Model to Liquid Mercury, High Temp 51 (1): 40-48. doi: 10.1134/S0018151X13010021

Bomont, J.M. and Bretonnet, J.L. (2006). An Effective Pair Potential for Thermodynamics and Structural Properties of Liquid Mercury. J. Chem. Phys. 124 (5): 054504. doi: 10.1063/1.2166384

Bui, K., and Akkutlu, I.Y. (2015). Nanopore Wall Effect on Surface Tension of Methane. J. Molecular Physics. 113 (22): 3506-3513. doi: 10.1080/00268976.2015.1037369

Bui, K. and Akkutlu, I. Y. (2016). Hydrocarbons Recovery from Model-Kerogen Nanopores. SPE Journal SPE-185162-PA (in press; posted 12 Dec. 2016). doi: 10.2118/185162-PA

Bustin R.M., Bustin A.M.M., Cui A., Ross, D., and Pathi, V.M. (2008). Impact of Shale Properties on Pore Structure and Storage Characteristics. SPE 119892 presented at SPE shale gas production conference in Fort Worth, Texas; November 16-18

Chen, J.Y., Kutana, A., Collier, C.P., and Giapis, K.P. (2005). Electrowetting in Carbon Nanotubes. Science 310 (5753): 1480-1483. doi: 10.1126/science.1120385

Clarkson C.R., Jensen J.L., Blasingame T.A. (2011). Reservoir Engineering for Unconventional Gas Reservoirs: What Do We Have to Consider? SPE-145080-MS presented at SPE North American Unconventional Gas Conference and Exhibition in Woodlands, Texas; June 12–16

Clarkson, C.R., Solano, N., Bustin, R.M., Bustin, A.M.M., Chalmers, G.R.L., He, L., Melnichenko, Y.B., Radliński, A.P., and Blach, T.P. (2013). Pore Structure Characterization of North American Shale Gas Reservoirs using USANS/SANS, Gas Adsorption, and Mercury Intrusion. Fuel 103: 606-616. doi: 10.1016/j.fuel.2012.06.119

Coates, G.R., Xiao, L., and Manfred, G.P. (1999). NMR Logging Principles and Applications: Halliburton Energy Services Publication H02308.

Coates, G. R., Miller, M., Gillen, M., and Henderson, C. (1991). The MRIL in Conoco 33-1—An Investigation of a New Magnetic Resonance Imaging Log, paper presented at SPWLA 32nd Annual Logging Symposium in Midland, Texas; June 16-19

Feng, F. and Akkutlu, I.Y. (2015). Flow of Hydrocarbons in Nanocapillary: A Non-Equilibrium Molecular Dynamics Study. SPE-177005, paper presented at the SPE Asia Pacific Unconventional Resources and Exhibition held in Brisbane, Australia, November 9-11

Giesche, Herbert. (2006). Mercury Porosimetry: A General (Practical) Overview. Part. Part. Syst. Charact. 23: 9-19. doi: 10.1002/ppsc.200601009.

Hinchliffe, A. (2003). Molecular Modelling for Beginners (2nd ed.): John Wiley & Sons Ltd.

Holman, G.J.F., and ten Seldam, C.A. (1994). A Critical Evaluation of the Thermophysical Properties of Mercury. J. Phys. Chem. Ref. Data. 23 (5), 807. doi: 10.1063/1.555952

Iakovlev, A., Bedrov, D., and Müller, M. (2015). Surface Tension of Liquid Mercury: A Comparison of Density-dependent and Density-independent Force Fields. Euro. Phys. J. B. 88: 323. doi: 10.1140/epjb/e2015-60594-2

Josh, M., Esteban, L., Delle Piane, C., Sarout, J., Dewhurst, D.N., and Clennell, M.B. (2012). Laboratory Characterization of Shale Properties. J. Petrol. Sci. Eng. 88-89: 107-124. doi: 10.1016/j.petrol.2012.01.023

Kalová, J. and Mareš, R. (2015). Size Dependences of Surface Tension. Int. J. Thermophys. 36 (10): 2862-2868. doi: 10.1007/s10765-015-1851-1

Keighin, C.W. (1997). Physical Properties of Clastic Reservoir Rocks in the Uinta, Wind River, and Anadarko Basins, As Determined by Mercury-injection Porosimetry. USGS Bull. 2146: 73-83

Kou, R. Alafnan, S.F.K. and Akkutlu, I.Y. (2016). Multi-scale Analysis of Gas Transport in Kerogen, accepted for publication in the Journal of Transport in Porous Media (in press: posted 28 October 2016). DOI 10.1007/s11242-016-0787-7

Kuila U. and Prasad M. (2013). Specific Surface Area and Pore-size Distribution in Clays and Shales. Geophysical Prospecting. 62 (1): 341-362. doi: 10.1111/1365-2478.12028

Kutana, A. and Giapis, K.P. (2007). Contact Angles, Ordering, and Solidification of Liquid Mercury in Carbon Nanotube Cavities. Phys. Rev. B 76: 195444. doi: 10.1103/PhysRevB.76.195444

Loucks, R.G., Reed, R.M., Ruppel, S.C., and Hammes, U. (2012). Spectrum of Pore Types and Networks in Mudrocks and A Descriptive Classification for Matrix-related Mudrock Pores. AAPG Bulletin. 96 (6): 1071-1098. doi: 10.1306/08171111061

Loucks, R.G., Reed, R.M., Ruppel, S.C., and Jarvie, D.M. (2009). Morphology, Genesis, and Distribution of Nanometer-Scale Pores in Siliceous Mudstones of the Mississippian Barnett Shale. Jour. Sedimentary Research. 79 (12): 848-861. doi: 10.2110/jsr.2009.092

Lu, H.M. and Jiang, Q. (2005). Size-Dependent Surface Tension and Tolman's Length of Droplets. Langmuir 21 (2): 779–781. doi: 10.1021/la0489817

Plimpton, S. (1995). Fast Parallel Algorithms for Short-Range Molecular Dynamics. J. Comput. Phys. 117 (1): 1-19 (http://lammps.sandia.gov). Lammps manual.

Purcell, W.R. (1949). Capillary Pressures - Their Measurement Using Mercury and the Calculation of Permeability. Journal of Petroleum Technology 1 (2): 39-48. doi:10.2118/949039-G

Rahmani Didar, B. and Akkutlu, I.Y. (2013). Pore-size Dependence of Fluid Phase Behavior and Properties in Organic-rich Shale Reservoirs. SPE-164099-MS, paper presented at the SPE Int. Symposium on Oilfield Chemistry held in Woodlands, Texas, USA, 8-10 April. doi:10.2118/164099-MS

Rezaee, R., Saeedi, A., and Clennell, B. (2012). Tight Gas Sands Permeability Estimation from Mercury Injection Capillary Pressure and Nuclear Magnetic Resonance Data. J. Pet. Sci. Eng. 88–89: 92–99. doi: 10.1016/j.petrol.2011.12.014

Riewchotisakul, S., and Akkutlu, I. Y. (2016). Adsorption Enhanced Transport of Hydrocarbons in Organic Nanopores. SPE-175107-MS, paper presented at the SPE

Annual Technical Conference and Exhibition held in Houston, Texas, USA, 28-30 September. doi: 10.2118/175107-MS

Rigby, S.P. and Edler, K.J. (2002). The Influence of Mercury Contact Angle, Surface Tension, and Retraction Mechanism on the Interpretation of Mercury Porosimetry Data, J Colloid Interface Sci. 250 (1): 175–190. doi: 10.1006/jcis.2002.8286

Sigal, R.F. (2015). Pore-Size Distributions for Organic-Shale-Reservoir Rocks from Nuclear-Magnetic-Resonance Spectra Combined with Adsorption Measurements. SPE J. 20 (4): 824-830. doi:10.2118/174546-PA

Tolman, R.C. (1949). The Effect of Droplet Size on Surface Tension. J. Chem. Phys. 17 (3): 333–337. doi: 10.1063/1.1747247

Wang, J.Y., Betelu, S. and Law, B.M. (2001). Line Tension Approaching a First-order Wetting Transition: Experimental Results from Contact Angle Measurements. Phys. Rev. E 63: 031601. doi: 10.1103/PhysRevE.63.031601

Wang, S., Javadpour, F., and Feng, Q. (2016). Confinement Correction to Mercury Intrusion Capillary Pressure of Shale Nanopores. Sci. Rep., 6: 20160. doi: 10.1038/srep20160

Washburn E.W. (1921). The Dynamics of Capillary Flow. Physical Review 17: 273. doi: 10.1103/PhysRev.17.273

Werder, T., Walther, J. H., Jaffe, R. L., Halicioglu, T. and Koumoutsakos, P. (2003). On the Water-Carbon Interaction for Use in Molecular Dynamics Simulations of Graphite and Carbon Nanotubes. J. Phys. Chem. B 107 (6): 1345–1352. doi: 10.1021/jp0268112

Zumdahl, S.S., and Zumdahl, S.A. (2007). Chemistry (7th ed.): Houghton Mifflin.

APPENDIX A

DERIVATION OF THE YOUNG-LAPLACE EQUATION

Consider capillary rise problem shown in Figure A1. At point A, the total energy change

(ΔE_h) that is associated with the formation of the liquid column of height h is:

$$\Delta E_{total} = \Delta E_s + \Delta E_v \qquad\qquad\text{A1}$$

where ΔE_s and ΔE_v are the changes in surface energy and the potential energy,

respectively. Inside the capillary, the surface energy ΔE_s associated with the capillary rise

can be expressed as follows:

$$\Delta E_s = 2\pi r \cdot (\sigma_{sl} - \sigma_{sv})h \qquad\qquad\text{A2}$$

where r is the inner radius of the tube, σ_{sl} the solid- liquid surface tension and σ_{sv} the

solid-vapor surface tension. The potential energy ΔE_v can be expressed as:

$$\Delta E_v = \frac{1}{2}\pi r^2 \rho hgh = \frac{1}{2}\pi r^2 \rho h^2 g \qquad\qquad\text{A3}$$

where ρ is the density of the liquid in the tube, g acceleration of the gravity. Substituting

equation (A2) and (A3) into equation (A1), equation (A4) is obtained representing the

change in energy associated with the capillary rise:

$$\Delta E_{total} = 2\pi r \cdot (\sigma_{sl} - \sigma_{sv})h + \frac{1}{2}\pi r^2 \rho h^2 g \qquad\qquad\text{A4}$$

It should be noted that the solid-vapor surface tension always has a larger value than the

solid-liquid surface tension, and thus the first term on the right side of equation (A4) is a

negative value. As a result, in capillary rise, the gravitational energy, which is the second

term on the right side, is always opposing the rise. Before reaching the equilibrium height,
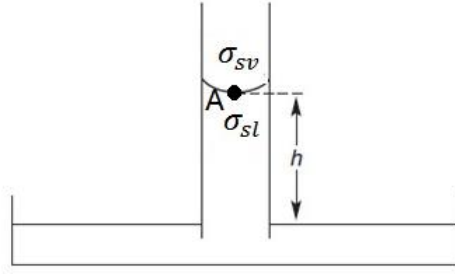
Figure A1. Capillary rise of a liquid in an open cup in contact with air

h^*, the total energy would decrease, and, finally, when it reaches the minimum energy, we have:

$$\frac{\partial \Delta E_{total}}{\partial h} = 2\pi r \cdot (\sigma_{sl} - \sigma_{sv}) + \pi r^2 \rho h^* g = 0 \qquad \text{A5}$$

Solving for h^*:

$$h^* = -\frac{2(\sigma_{sl} - \sigma_{sv})}{r\rho g} \qquad \text{A6}$$

The height of the liquid in the capillary would change until it reaches h^*. Additionally, as it was explained before, the term $(\sigma_{sl} - \sigma_{sv})$ has a negative value for a system showing capillary rise, therefore the equilibrium height h^* becomes positive. More commonly, this equilibrium height can be expressed in terms of the liquid-vapor surface tension σ_{lv} and the contact angle θ as follows:

Based on Figure A2, we can express the force balance in the y direction as:

$$\sigma_{sv} = \sigma_{sl} + \sigma_{lv}cos\theta \qquad \text{A7}$$
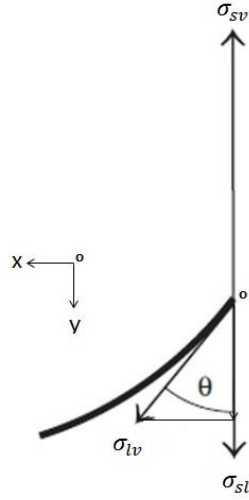
Figure A2: Balance of surface forces as the vectors originating from the

intersection point

Here, σ_{lv} is the liquid-vapor surface tension, θ the contact angle of the liquid-vapor interface. Substituting equation (A7) into equation (A6), we would obtain:

$$h^* = -\frac{2[(\sigma_{sv} - \sigma_{lv}cos\theta) - \sigma_{sv})]}{r\rho g} = \frac{2\sigma_{lv}\cos\theta}{r\rho g} \qquad \text{A8}$$
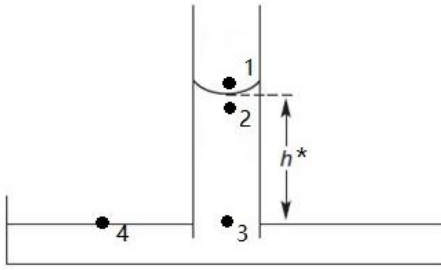
Thus,

$$\rho g h^* = \frac{2\sigma_{lv}\cos\theta}{r} \qquad \text{A9}$$

The pressure difference ΔP exisiting in both sides of the liquid-vapor interface is the definition of the capillary pressure P_c, and we have:

$$\Delta P = P_2 - P_1 = P_c \qquad \text{A10}$$

As shown in Figure A3, because $P_1 = P_4$ =atmospheric pressure, and $P_3 = P_4$ due to the same level, thus $P_1 = P_3$. Hence, we also have:

Figure A3: Capillary rise at equilibrium state when h = h*

$$P_c = P_2 - P_3 = \rho g h^*$$
<div align="right">A11</div>

Because the pressure difference between the Point 2 and 3 can be rewrite as:

$$P_2 - P_3 = \rho g h^*$$
<div align="right">A12</div>

Thus, we have:

$$P_c = \rho g h^*$$
<div align="right">A13</div>

Combining equation (A9) and (A13) we finally have:

$$P_c = \frac{2\sigma_{lv} \cos \theta}{r}$$
<div align="right">A14</div>

Moreover, when we have two immiscible liquids, we should have:

$$P_c = \frac{2\gamma \cos \theta}{r\rho g}$$
<div align="right">A15</div>

where γ is the interfacial tension of two immiscible liquids.